Plasmonic Nanoparticles and Their Suspensions for Solar Energy Conversion

by

Wei Lv

A Thesis Presented in Partial Fulfillment
of the Requirements for the Degree
Master of Science

Approved May 2012 by the
Graduate Supervisory Committee:

Patrick Phelan, Chair
Lenore Dai
Ravi Prasher

ARIZONA STATE UNIVERSITY

August 2012

ABSTRACT

Plasmon resonance in nanoscale metallic structures has shown its ability to concentrate electromagnetic energy into sub-wavelength volumes. Metal nanostructures exhibit a high extinction coefficient in the visible and near infrared spectrum due to their large absorption and scattering cross sections corresponding to their surface plasmon resonance. Hence, they can serve as an attractive candidate for solar energy conversion. Recent papers have showed that dielectric core/metallic shell nanoparticles yielded a plasmon resonance wavelength tunable from visible to infrared by changing the ratio of core radius to the total radius. Therefore it is interesting to develop a dispersion of core-shell multifunctional nanoparticles capable of dynamically changing their volume ratio and thus their spectral radiative properties. Nanoparticle suspensions (nanofluids) are known to offer a variety of benefits for thermal transport and energy conversion. Nanofluids have been proven to increase the efficiency of the photo-thermal energy conversion process in direct solar absorption collectors (DAC). Combining these two cutting-edge technologies enables the use of core-shell nanoparticles to control the spectral and radiative properties of plasmonic nanofluids in order to efficiently harvest and convert solar energy. Plasmonic nanofluids that have strong energy concentrating capacity and spectral selectivity can be used in many high-temperature energy systems where radiative heat transport is essential. In this

thesis， the surface plasmon resonance effect and the wavelength tuning ranges for different metallic shell nanoparticles are investigated, the solar-weighted efficiencies of corresponding core-shell nanoparticle suspensions are explored, and a quantitative study of core-shell nanoparticle suspensions in a DAC system is provided. Using core-shell nanoparticle dispersions, it is possible to create efficient spectral solar absorption fluids and design materials for applications which require variable spectral absorption or scattering.

ACKNOWLEDGEMENT

I would like to express my gratitude to my advisor Dr. Patrick Phelan for his valuable guidance, discussions and financial support during my graduate study. Without him, I won't step into the nano-science world.

I also would like to thank Dr. Lenore Dai, Dr. Ravi Prasher for being my thesis defense committee members and reviewing my thesis.

I am very grateful to Dr. Robert Taylor for helping me at the beginning of my research and continuous encouragement. I also want to thank Dr. Todd Otanicar for sharing codes. Thanks to Dr. Rajasekaran Swaminathan for his reviews on my paper.

I would like to thank my parents, my family and my friends for their encouragement and support. I would also like to thank my 'lab mates' - Karthik, Moxuan, Andrey, Willie, and Mark, for all the great discussions, revision and help along the way.

Especially, I would like to give my special thanks to my girlfriend Quan Yuan who accompanies me all along for two years of master study. Her grand love and meticulous care enabled me to complete this thesis work.

TABLE OF CONTENTS

Page

Page

Page

LIST OF TABLES

Table Page

LIST OF FIGURES

Figure Page

Figure Page

Nomenclature

A_m	Solar-weighted absorption coefficient
A_R	Area [m^2]
c_0	Specific heat
C	Cross section [m^2]
D	Mean particle diameter [nm]
E_λ	Spectral solar irradiance [W $m^{-2}um^{-1}$]
E_i	Electric field (i=0, 1, 2, 3)
f_v	Volume fraction [%]
G	Incident solar flux on the collector plan [W m^{-2}]
h	Planck constant [J s]
h	Hear transfer coefficient [W $m^{-2}K^{-1}$]
H	Thickness of the solar collector
I	Intensity [W m^{-2} str^{-1} μm^{-1}]
k	Thermal conductivity [W $m^{-1}K^{-1}$]
k	Imaginary component of refractive index
k_B	Boltzmann Constant [J K^{-1}]

ℓ	Mean free path [m]
L	Length of the solar collector
m	Normalized complex refractive index
$\dot{m}$	Mass flow rate [kg s^{-1}]
n	Real component of refractive index
q_r	Radiative flux [W m^{-2}]
Q	Scattering or absorption efficiency
S	Incoming solar radiation [W m^{-2} μm^{-1}]
T	Temperature [K]
U	Velocity [m s^{-1}]
r	Particle radius [nm]
V_f	Fermi velocity [m/s]

Subscripts

Abs	Absorption
bo	Bound electron
bulk	Bulk material property

eff	Effective
ext	Extinction
exp	Experimental
i	Directional
in	Collector inlet
out	Collector outlet
w	Wall
g	Glass
sca	Scattering
p	Plasmon
∞	Bulk material property

Greek Symbols

α	Polarizability
ε'	Real component of dielectric constant, [F/m or kg mm / (mV^2 s^2)]
ε''	Imaginary component of dielectric constant, [F/m or kg mm / (mV^2 s^2)]
λ	Wavelength, [μm]

σ	Extinction coefficient, [1/m]
γ	Relaxation frequency
∂	Size parameter
τ_0	Free electron scattering time

CHAPTER 1 INTRODUCTION

1) Overview

Research in this thesis is focused on energy transport and conversion in nanoparticle laden fluids, commonly called "nanofluids." Plasmonics and nanofluids are two emerging areas that are receiving lots of attention recently. However, few studies have been done on plasmonic nanofluids which are promising in energy harvesting, microfluidics and optofluidics. In this work, I studied typical plasmonic nanostructures (solid metallic nanoparticles and core-shell nanoparticles), and their suspensions' spectral selective optical properties and their application to photo-thermal energy harvesting and conversion. The optical response of different kinds of plasmonic nanofluids is numerically analyzed and applied in a 2D combined radiation and convection model in a particulate-laden liquid film to predict the efficiency of a nanofluid-based direct solar energy collector.

2) Solar Energy

Fossil fuel has played an extraordinarily important role in energy systems for modern industries after the second industrial revolution. However, the reality that fossil fuel is not a sustainable energy source is widely accepted and of great

concern. The author does not provide any quantitative data for this fact that fossil fuel is unstable in the long term. However, I do want to emphasize it again since it is one of the motivations of this work and also for me to continue research in the energy field. What's more important, fossil-fuel-based energy systems have strong environmental effect by not only generating CO_2,which is a well-known 'Greenhouse Effect' gas, but also by polluting the environment by emitting other harmful gases. All these reasons make renewable energy an essential and imperative area of scientific research. Among available renewable and sustainable energy sources, the potential solar resource available is enormous and largely undeveloped. I believe a large amount of research efforts and investments will be directed towards growing the use of solar energy.

3) Nanofluids as a Transport and Participating Medium

Nanofluids are suspensions of nanoparticles (nominally 1-100 nm in size) in conventional base fluids such as water, oils or glycols. Nanofluids have seen a huge growth in popularity since they were proposed by Choi in 1995 [1]. Researchers have studied different aspects of nanofluids, including synthesis techniques [2,3], mass transport [4,5], boiling phenomena and critical heat flux enhancement [6–9], photo-thermal energy harvesting and conversion [10–14], optics [15–19], and electronics [20–22].

Within the realm of thermal science, nanofluids originally attracted attention for their inexplicably large effective thermal conductivities, which led to the idea of exploiting nanofluids as heat transfer fluids. Consequently, along with their thermal conductivity, k, specific heat, c_p, viscosity, μ, convective heat transfer coefficient, h, contribution to boiling heat transfer, critical heat flux and mass diffusivity and transfer coefficient are all of interest.

Compared to thermal conductivity and convection studies with nanofluids, the optical and radiative properties of nanofluids have received much less attention. However, very recently, the number of studies on radiative heat transfer in nanofluids has been growing[23–25]. This is due to the fact that, in general, a composite nanofluid has different properties than those found in either the base fluid or the particles. At high temperatures, knowledge of the resultant radiative properties becomes increasingly important.

Small particle absorption and scattering of light has drawn the attention of scientists long before nanofluid research became prevalent. Much of the current theory of small particle optical properties was developed over 100 years ago, amongst many great scientists, by Gustav Mie [26]. Several texts on absorption and scattering present great overviews on these topics (see, for example [27–29]). Kreibig and Vollmer [30] also present a good theoretical groundwork for the absorption and scattering of metallic small-scale particles. By 1970, the radiative

properties of small particles were starting to be applied to engineered systems - mostly in gas-particle mixtures [31–35].

In the last several years, though, contemporary nanofluids have been studied from the viewpoint of controlling optical and radiative properties. Among others, Phelan et al. [24,36–38]have shown that radiative and optical properties of nanofluids can be significantly altered from those of base fluid and that dependent scattering effects will be of great importance. One of the major advantages of going to a system that uses nanoparticle suspensions is the tunability of the size, shape, and volume fraction of the nanoparticles for the operating mode of the system. Small changes in these properties can drastically change scattering and absorption.

The basic concept of using particles to collect solar energy was first studied in the '70s with [32] and [39] who mixed particles in a gas working fluid. In the following years, gas-particle receivers were extensively modeled and several prototype collectors were built and tested. This research experimentally demonstrated the absorption of radiation volumetrically using particles [31,33,35,40–43]. However, in this work the particles were mixed with a gas - i.e. not a liquid. There are a few recent studies, however, which model and experiment with the concept of liquid-based nanofluid solar collectors [14,23,37,44–52].

A solar thermal collector using a dispersion of nanoparticles acting as a direct solar receiver [53–55] is one promising application. In conventional solar thermal collectors, the sunlight is absorbed onto a surface which heats up, then transfers the heat to a working fluid. Direct absorption is a volumetric approach in which radiation is absorbed within a liquid film, which has three distinct advantages over conventional surface-based approaches: first, the absorption of incoming energy in a nanoparticle suspension goes beyond that of surface absorption of a similar material [49], second, the overall thermal resistance can be reduced by reducing the need for convection heat transfer between the absorbing surface and the working fluid [14], and third, the thermal conductivity and convective heat transfer of nanofluids play a positive role in thermal energy transport.

One of the main outcomes of this work is that the resultant optical properties of the fluid must be controlled precisely. An unstable or improperly designed nanofluid could actually be detrimental in a solar collector. For example, if the volume fraction of nanoparticles is very high, all the incoming light is absorbed in a thin surface layer where the thermal energy is easily lost to the environment. On the other hand, if the volume fraction of nanoparticles is low, the nanofluid cannot absorb all the incoming solar radiation. From an applications point of view, the most important parameters to control are the particle volume fraction, f_v, the particle size parameter, α, and the resultant extinction coefficient, σ. The particle

size parameter is a non-dimensional quantity that relates the particle diameter to the wavelength of incident light and is defined as [29]:

$$\alpha = \frac{\pi D}{\lambda}$$

Using these parameters, on a regime map how solar absorbing nanofluids compare with other common particulate mediums can be shown. Figure 1 adapted from Tien [35], shows this comparison.

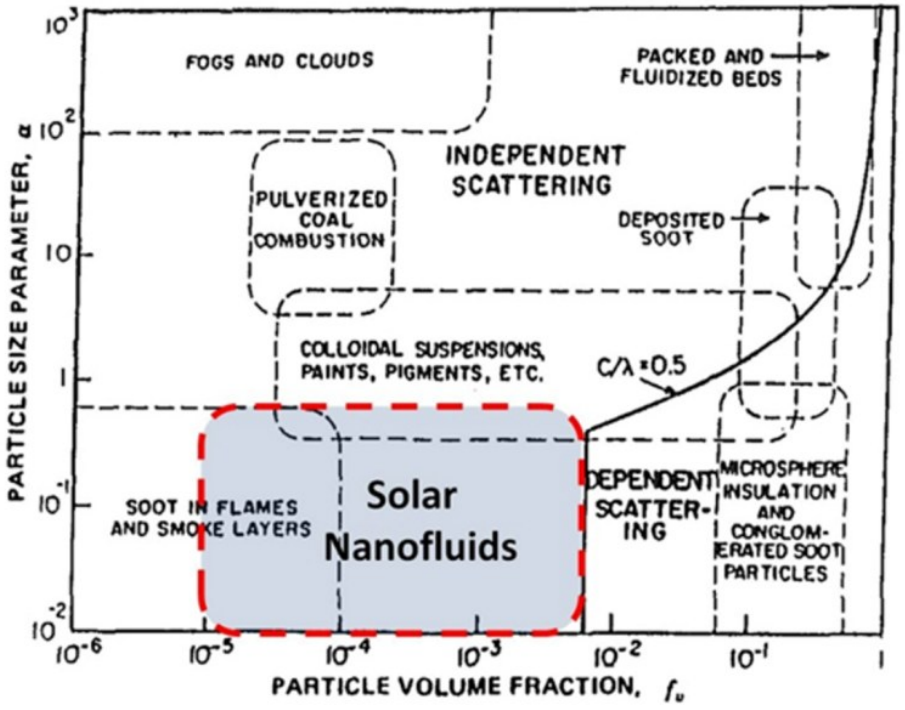

Figure 1 Scattering regime map showing the boundary between dependent and independent scattering

For most nanofluid-based solar collectors, volume fractions are low, but greater than that of smoke or soot in flames. At the same time the particles are usually orders of magnitude smaller than paints, pigments, or pulverized coal.

With very small, far-apart particles, scattering is small. If the particles are made of graphite or metals the absorption is high. This means that the extinction coefficient results almost entirely from absorption. In comparison with incoming solar energy, nanofluids make very good absorbers - relative to nominally transparent base fluids like water, oils, and molten salts.

Overall, nanofluids provide a promising path to increase the efficiency of solar collection systems. Efficiency improvements of up to 10% have been theoretically and experimentally reported [14,49,54].

4) Plasmonic Nanoparticles

Metallic nanoparticles display a variety of interesting and useful optical and radiative properties – particularly around the plasmon resonance frequency. To understand plasmon resonance electrons are considered as being connected to the positive metal ions of the particle by a classical mass-spring-damper. Thus, for a given particle (material, size, shape, structure), there is a natural (plasmon resonance) frequency where incoming photons of that frequency cause large oscillations of the electrons. An analogous situation would be natural frequency wind loads causing large amplitude oscillations on a bridge. Unlike natural frequencies of a bridge, however, plasmon resonance can actually be very useful and beneficial. The motivating factor for doing this work with nanoparticles is

that electrons are confined within the small size of the nanoparticle. This means that by picking the correct particle, the plasmon resonance frequency can be tailored to match the application. When the particle size is in nanoscale, the size effect needs to be considered. What's more, the core-shell nanostructure which couples the core/shell and shell/medium surface plasmon resonance together could increase the tunability of the nanostructures.

In fact, there are many applications of plasmon resonance with nanoparticles by using their outstanding light concentrating capacity in electronics, biodetection , and catalysis [56]. For example, Carotenuto et al. used Ag–polymer nano-composites to fabricate UV-absorbers and color filters for advanced optical devices [57]; Tessier et al. used colloidal crystals to produce gold nanostructured films as active surfaces for surface-enhanced Raman spectroscopy [58]. Liu et. al. utilized plasmonic nanoparticles to increase the yield of photocatalytic water splitting [59]. Torkamani et al. applied the plasmon effect to aid microalgal growth [60]. There are also many sensing applications, chemical, biomolecule, and biological agent detection and identification. Sensing applications are usually carried out based on the refractive index dependence of plasmon resonance. Thus, measurements are optical – i.e. non-invasive - which is advantageous to sensitive bio-samples.

Neeves et al. [61] developed a numerical model which can predict plasmon resonance for composites of nanospheres with a metallic core and a nonlinear shell or with a nonlinear core and metallic shell suspended in a nonlinear medium. Averitt et al. [62] studied the linear optical properties of gold nanoshells consisting of a nanometer-scale dielectric core surrounded by a thin metallic shell. In their work, they synthesized gold-coated Au_2S nanoparticles and observed a plasmon resonance tunable from 600 to greater than 1000 nm by changing the shell/core diameter ratio. Halas et al. [63–65] explored plasma resonance and surface enhanced Raman scattering on different shaped metal/dielectric heteronanostructures. Kelly et al. [66] and N. G. Khlebtsov et al [16] performed calculations of the effect of size, shape, and structure of metal nanoparticles (sphere, spheroid, bisphere, and nanoshell) on the refractive index of disperse nanoparticle media. They numerically showed that variations in the shape and structure of a particle cause particle absorption and scattering changes as well as changes in the dependence of these spectra on the refractive index of the environment. Schatz's group [56,66,67] studied multiple higher-order plasmon resonances in colloidal cylindrical gold nanorods and silver nanoparticle arrays. Observable multi-pole resonance can be interpreted as a bar which only high quality, homogeneous nanostructures can pass.

In summary, controlled plasmon resonance has many possible applications. At this point, most of the basic concepts are still under investigation in laboratory situations. As new ideas and new fabrication techniques come to the forefront, however, this field for nanofluids can certainly be expected to expand.

CHAPTER 2 PLASMONIC NANOFLUIDS' OPTICAL PROPERTIES

5) Introduction

The radiative properties of nanoparticle suspensions (nanofluids) could have strong impacts on the absorption and emission of energy systems, especially at high temperatures when thermal radiation is an important heat transfer mode. One example is optimizing the harvesting of the solar spectrum by adjusting the optical properties of a core-shell nanoparticle suspension in a direct-absorption system [68]. Another example is in high-temperature energy storage where changing the emissivity can dramatically increase the heat transfer capacity of the working fluid.

The motivation for this study on the radiative control of dispersions comes first from the desire to establish fundamental knowledge on the ability to control the radiative properties. Another motivator is the potential applications to thermal energy systems. By dynamically altering the absorption/emission characteristics, it is possible to suit the changing needs of the given application. One such application could be a dual solar thermal collector during the day which could then be transitioned to a radiative cooling system at night (see Fig.2). This system would enable a much more efficient utilization of space since one system could achieve two objectives

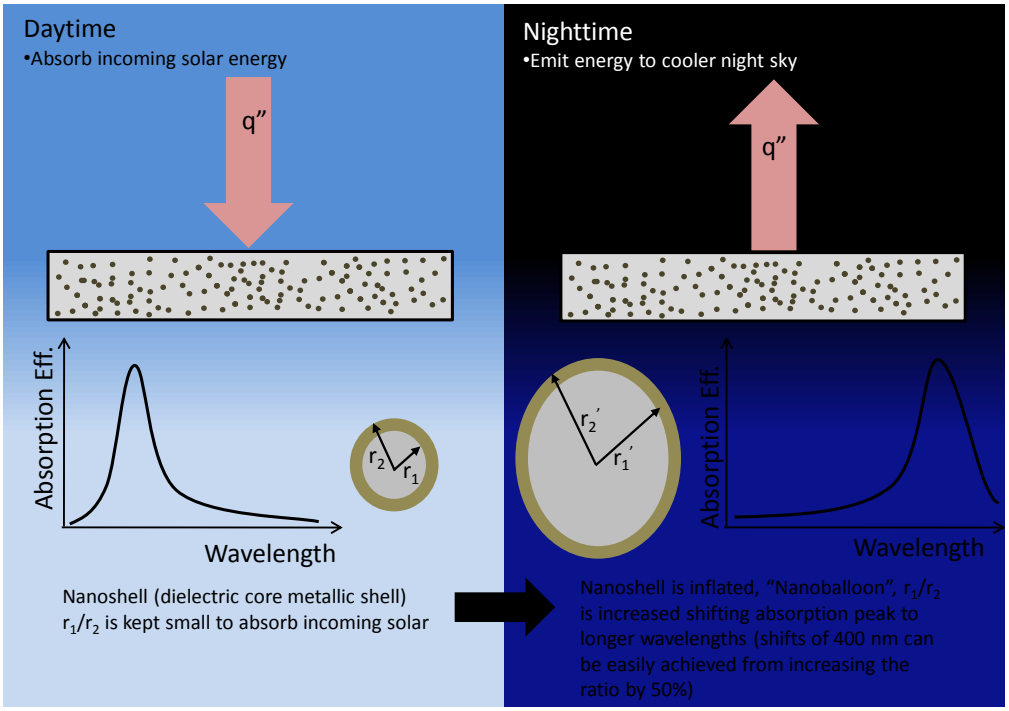

Figure 2 Dual use solar thermal collector/night sky radiator using core-shell multifunctional nanoparticle suspensions.

instead of requiring two separate systems. It could be applied, for example, in a solar thermal power plant to replace the cooling tower that consumes a large amount of water. Another possibility is to create a dynamic spectral liquid filter capable of absorbing or transmitting light upon activation.

In this chapter, the potential of nanoparticles are studied and I attempt to find the best nanostructures whose optical properties can be dramatically altered and dynamically controlled. The choices of the particle material and particle shape are two simple methods to change the spectral properties of nanofluids [69] which directly impact the spectral response. One possible method for changing the

spectral properties of nanofluids is through controlling the size of core-shell nanoparticles, which combines diverse core and shell materials [70]. By using core-shell nanoparticles it is possible to dynamically switch the radiative properties of nanofluids. Lee et al. [68] recently showed that a mixture of different-sized gold nanoshells in water-based nanofluids will harvest more solar spectrum than aluminum nanofluids, and will increase the efficiency of a direct solar receiver. However, for a high flux solar collector of a concentrated solar power plant, using gold nanomaterial is not an economic choice. In this chapter, "cheap" metal core-shell nanoparticles suspended in fluids are proven to have equivalent solar harvesting capacity as gold nanoshells.

6) Modeling the Optical Response of Core-Shell Nanoparticle Suspensions

Figure 3 is the geometric scheme of a core-shell nanoparticle. In this study, the core is made of a dielectric material (Si), and the shell is made of metallic material (Ag, Au, Al, or Cu). These materials could be modified for the specific absorption and radiation values required. When applying an electromagnetic field, free electrons and bound electrons will interact with the field. Surface plasmon resonance (SPR) is caused by the confining force of free conduction electrons. Under specific conditions of wavelength, polarization and incident angle, free electrons (or plasma) at the surface of the nanoparticles absorb incident photons, converting them into surface plasmon waves, which spread across the surface. The large optical polarization associated with the surface plasmon resonance (SPR) brings on a vast local electric field boost at the nanoparticle surface as well as strongly enhanced light absorption and scattering by the nanoparticle at the SPR frequency [71]. The core-shell nanoparticles' SPR frequency depends on particle size, shape, shell thickness and the dielectric properties of the core and surrounding media [72]. In this application, materials which have a large range of spectral tunability from the visible to the infrared wavelengths are desired.

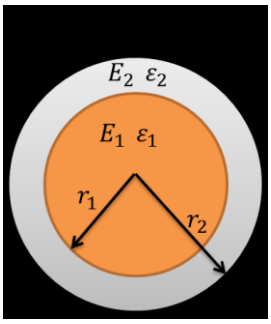

Figure 3 Core-shell nanoparticle geometry; $\varepsilon_i(1,2,3)$ are dielectric functions for the core, shell, and embedding regions, r_1, r_2 the core and shell radii and $r_2 - r_1$ the shell thickness. $E_i(1,2,3)$ are the electromagnetic fields in the core, the shell and the embedding media, respectively.

Various calculations and models have been made on the impact of an electromagnetic field on the spectral and optical properties of core-shell nanoparticles [61,62,73]. Two assumptions are widely accepted in most models. The first assumption is that the nanoparticle diameter is much smaller than the wavelength of the incident field. There are two major reasons for choosing this small size of nanoparticles. First of all, in a nanofluid-based absorption system, the absorption cross section is more important than the scattering cross section. Although the absorption cross section will increase with the particle size, scattering will increase more rapidly which is not favorable in an independent scattering system. Here I constrain the scattering cross section (C_{sca}) to be one order of magnitude smaller than the absorption cross section (C_{abs}), $C_{sca} / C_{abs} \le 0.1$.

Although different materials yield different results, this constraint ensures the radius is smaller than 50nm for most materials. Another important reason is for the stability of the dispersion of the nanofluids. Larger-sized nanoparticles (radius >100nm) will tend to fall out of the base fluid because of gravity. Since most of the incident light from the sun has a wavelength that is at least 10 times larger than the nanoparticle diameter, we can omit higher order terms in the Mie scattering solution and the approximation of Rayleigh scattering ($\pi \mathrm{D} / \lambda << 1$) is applicable. However, this assumption will not be accurate when the diameter of the core shell nanoparticle exceeds 50 nm. For larger particles, higher order multipoles—especially quadrupole plasmon resonance—should be considered [74]. In this work, the size of core-shell nanoparticles is limited to those smaller than 50 nm. The second assumption is that the incident field does not vary spatially over the diameter of the metallic shell and excitations due to the magnetic field are negligible. If the above two assumptions are appropriate, the so-called quasi-static approximation [62] is appropriate to use.

From Maxwell's equations, the scalar potential $\phi_1(r,\theta), \phi_2(r,\theta), \phi_3(r,\theta)$ can be derived inside the core, shell and embedding material, and the following equations are obtained[27]:

$$\overrightarrow{E_1} = -\nabla \varphi_1, \overrightarrow{E_2} = -\nabla \phi_2 \tag{1}$$

$$\nabla^2\phi_1 = 0(r < r_1), \nabla^2\phi_2 = 0(r_1 < r < r_2), \nabla^2\phi_3 = 0(r > r_2) \tag{2}$$

$$\phi_1 = \phi_2, \varepsilon_1 \frac{\partial \phi_1}{\partial r} = \varepsilon_2 \frac{\partial \phi_2}{\partial r}(r = r_1) \tag{3}$$

$$\phi_2 = \phi_3, \varepsilon_2 \frac{\partial \phi_2}{\partial r} = \varepsilon_3 \frac{\partial \phi_3}{\partial r}(r = r_2) \tag{4}$$

$$\lim_{t\to\infty} \phi_3 = -E_0 r\cos\theta = -E_0 z \tag{5}$$

Solving the linear Laplace equations yields [61],

$$\mathbf{E}_1 = \frac{9\epsilon_2\epsilon_3}{\epsilon_2\epsilon_a + 2\epsilon_3\epsilon_b} E_0[\cos(\Theta)\hat{e}_r - \sin(\Theta)\hat{e}_\theta]. \tag{6}$$

$$\begin{aligned}\mathbf{E}_2 = {} & \frac{3\epsilon_3}{\epsilon_2\epsilon_a + 2\epsilon_3\epsilon_b}[(\epsilon_1 + 2\epsilon_2) + 2(\epsilon_1 - \epsilon_2)(r_1/r)^3]E_0\cos(\Theta)\hat{e}_r \\ & - \frac{3\epsilon_3}{\epsilon_2\epsilon_a + 2\epsilon_3\epsilon_b}[(\epsilon_1 + 2\epsilon_2) - (\epsilon_1 - \epsilon_2)(r_1/r)^3]E_0\sin(\Theta)\hat{e}_\theta,\end{aligned} \tag{7}$$

$$\begin{aligned}\mathbf{E}_3 = {} & \left(2\frac{\epsilon_2\epsilon_a - \epsilon_3\epsilon_b}{\epsilon_2\epsilon_a + 2\epsilon_3\epsilon_b}\frac{{r_2}^3}{r^3} + 1\right)E_0\cos(\Theta)\hat{e}_r \\ & + \left(\frac{\epsilon_2\epsilon_a - \epsilon_3\epsilon_b}{\epsilon_2\epsilon_a + 2\epsilon_3\epsilon_b}\frac{{r_2}^3}{r^3} - 1\right)E_0\sin(\Theta)\hat{e}_\theta\end{aligned} \tag{8}$$

where $\varepsilon_a, \varepsilon_b$ are the effective dielectric functions and P the ratio of shell volume to total particle volume:

$$\varepsilon_a \equiv \varepsilon_1(3-2P) + 2\varepsilon_2 P \tag{9}$$

$$\varepsilon_b \equiv \varepsilon_1 P + \varepsilon_2(3-P) \tag{10}$$

$$P \equiv 1-(r_1 / r_2)^3 \tag{11}$$

The field of the composite particle in the region outside the sphere is the same as that of a dipole of effective moment

$$\phi_3 = \frac{\vec{p}.\vec{r}}{4\pi\varepsilon_3 r^3} \tag{12}$$

$$p = \varepsilon_3 \alpha E_0 \tag{13}$$

where the polarizability α is defined as

$$\alpha = 4\pi\varepsilon_0 r_2^3 \frac{\varepsilon_2\varepsilon_a - \varepsilon_3\varepsilon_b}{\varepsilon_2\varepsilon_a + 2\varepsilon_3\varepsilon_b} \tag{14}$$

From Rayleigh scattering theory, the relation between absorption, scattering cross section and the polarizability [27] is obtained as

$$C_{sca} = \frac{k^4}{6\pi}|\alpha|^2 \tag{15}$$

$$C_{abs} = k\mathrm{Im}(\alpha) \tag{16}$$

where $K = \frac{2\pi}{\lambda}\vec{n}$; Then inserting equation (14) into the above two equations leads to the scattering and absorption cross-sections of Rayleigh-regime particles [61]:

$$C_{sca} = \frac{k^4}{6\pi}|\alpha|^2 = \frac{128\pi^5}{3\lambda}\varepsilon_3^2 r_2^6 \left|\frac{\varepsilon_2\varepsilon_a - \varepsilon_3\varepsilon_b}{\varepsilon_2\varepsilon_a + 2\varepsilon_3\varepsilon_b}\right|^2 \quad (17)$$

$$C_{abs} = k\,\mathrm{Im}(\alpha) = \frac{8\pi^2\sqrt{\varepsilon_3}}{\lambda} r_2^3\,\mathrm{Im}\left(\frac{\varepsilon_2\varepsilon_a - \varepsilon_3\varepsilon_b}{\varepsilon_2\varepsilon_a + 2\varepsilon_3\varepsilon_b}\right) \quad (18)$$

Then it is possible to calculate the extinction efficiency Q_{ext} of a single nanoparticle from

$$Q_{ext} = (C_{abs} + C_{sca}) / \pi r_2^2 \quad (19)$$

Previously the optical properties of solar nanofluids based on solid nanoparticles [37] were analyzed. After calculation of the single-particle extinction efficiency, the properties of the total fluid mixture could be worked out based on the particle concentration. At higher particle concentrations, > 0.6% volume fraction, complicated dependent and multiple scattering phenomena can have severe effects since there would be a lot of closely packed particles [75]. It turns out that effective direct solar absorption collection can be achieved for nanofluids of < 0.6% volume fraction when the solar collection has sizable absorption path lengths (>1 mm) [37]. Hence, for solar collectors only independent scattering is needed to be considered which makes it easier to analyze the optical properties. When multiple scattering is negligible, the

extinction coefficient of the nanoparticles is calculated from the absorption and scattering efficiencies[27]:

$$\sigma_{particle} = \frac{3 f_v Q_{ext}}{2D} \tag{20}$$

where D is particle diameter. After computing the nanoparticles' extinction coefficient in nanofluids, it is necessary to add in the absorption of the base fluid. In this model, water is chosen as the base fluid which is actually a good absorber in the near infrared and infrared region.

A recent study [37] reported a first-order method to analyze the nanofluids' total extinction coefficient, which is found from a simple addition of the base fluid extinction coefficient, σ_{fluid}, and that of all the particles, $\sigma_{particle}$:

$$\sigma_{nanofluid} = \sigma_{particle} + \sigma_{fluid} \tag{21}$$

where the basefluid extinction coefficient is determined through:

$$\sigma_{fluid} = \frac{4\pi k_{fluid}}{\lambda} \tag{22}$$

The same approach is applied here, in the results to follow.

In order to calculate the absorption and scattering cross sections of a core-shell nanoparticle, it is required to get the dielectric function of a metallic shell. The optical properties of the bulk metallic material are determined from Palik [76]. However the dielectric function of nanoscale metallic particles is size

dependent, and can be considerably different from that of the bulk material. Thus it is necessary to modify the bulk properties to include the impact of size-dependent effects on the nanoparticle optical properties by the Drude-Sommerfeld model[29]. When the dimension of the nanoparticle decreases below the mean free path of the bulk material, the surface causes additional scattering, hence the optical properties need to be modified. This effect has been demonstrated numerically [30], and confirmed experimentally for metallic nanoparticles [62]. The Drude-Sommerfeld model is adapted to model the size effect of metallic nanoparticles using [30]:

$$\varepsilon(\omega) = 1 - \omega_p^2 \frac{1}{\omega^2 + i\omega\gamma_{bulk}} \tag{23}$$

where ω_p is the bulk plasmon frequency, ω the frequency of the electromagnetic wave, and γ_{bulk} the relaxation frequency of the bulk metal. When the particle size is below the mean free path, the oscillations of the free electrons begin to interact with the particle boundary. This effect results in a modification to the electron decay time $\tau \equiv 1/\gamma$ which is particle size dependent for small particles [77]:

$$1/\tau_{eff} = 1/\tau_0 + AV_f / l_{eff} \tag{24}$$

where τ_{eff} is the effective relaxation time, τ_0 the bulk metal free electron scattering time, A a geometric parameter ranging from 2 to 1 in our model (I assume it to be 1), V_f the Fermi velocity, where the experimental value $V_f = 1.38 \times 10^6 m/s$ is used for gold nanoparticles [78], and l_{eff} the effective mean free path used in the determination of the decay time $\tau(l)$. For core-shell nanoparticles, I use a model proposed by Granqvist and Hunderi [79]:

$$l_{eff} = \frac{1}{2}\left[(r_2 - r_1)(r_2^2 - r_1^2)\right]^{1/3} \tag{25}$$

The Drude model itself is sufficient to describe the optical response of most metals below the threshold for interband electron transitions, like aluminum. However, above this threshold, it needs to be coupled with interband absorption which is called the Lorentz model [61]. The Drude and Lorentz model has been experimentally [77] confirmed for gold, silver and copper. The combined Drude and Lorentz model is then [61]:

$$\varepsilon(\omega) = \varepsilon(\omega)_{\exp} + \omega_p^2 \frac{1}{\omega^2 + i\omega\gamma_{bulk}} - \omega_p^2 \frac{1}{\omega^2 + i\omega\gamma(l_{eff})} \tag{26}$$

For the dielectric core and surrounding dielectric media, the optical properties from literature [76] can be used. The size effect of the core is neglected here.

7) Results and Discussion

i. Size-ratio effect on a single particle

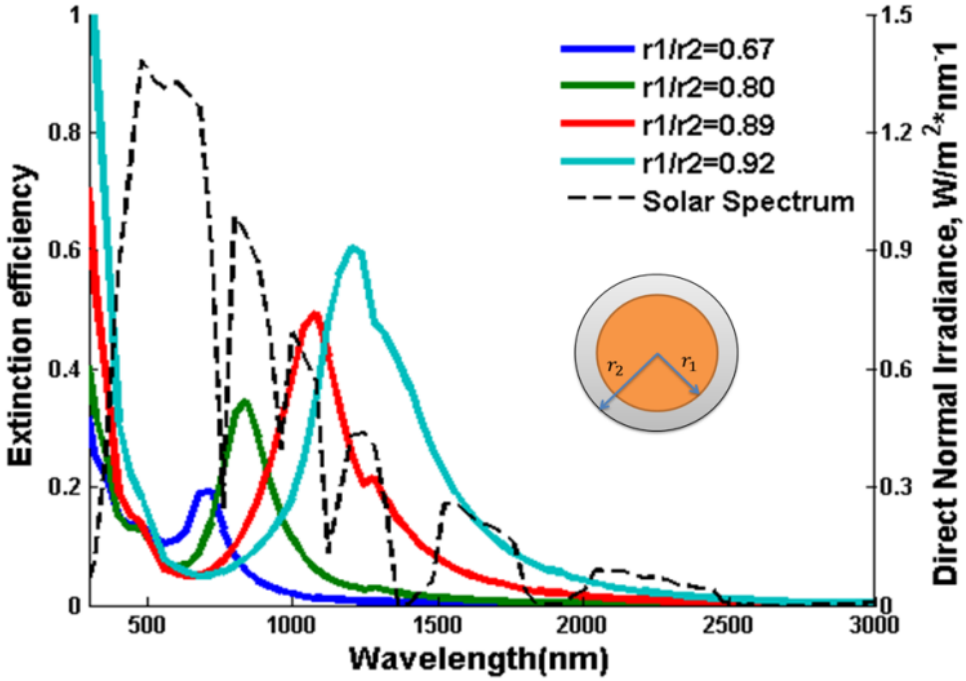

Figure 4 Individual Si core Au shell core-shell nanoparticle extinction efficiency (shell thickness $r_2 - r_1 = 2$ nm)

Figure 4 shows the potential red-shift effects caused by increasing the size ratio in a single particle. The shell thickness is set to be a constant (2 nm) for modeling simplicity. The total radius r_2 is varied continuously from 6 to 25 nm which keeps the calculations in the Rayleigh regime. The solar spectrum is also plotted to compare with the resonance frequency. From Fig. 4 a reasonable tuning range is observed (list in table 1). When the size ratio increases, the dipole

plasmon resonance wavelength shifts to longer wavelengths, which can be explained by equation (14), the definition of polarizability. When the denominator of equation (14) meets the condition at a certain wavelength, metallic dielectric core-shell nanoparticles demonstrate a dipolar plasmon resonance. After plugging equations (9-11) into equation (14), it is possible to solve for the dimension factor (r_1 / r_2), as a function of resonance frequency. For a specified core-shell nanoparticle, the plasmon resonance frequency is a function of the size ratio (if the shell and embedding medium are dielectrics). Then the following wavelength function is obtained [62]:

$$\frac{r_1}{r_2} = \left[1 + \frac{3}{2} \frac{\varepsilon_2^{'}(\lambda)(\varepsilon_1 + 2\varepsilon_3)}{\varepsilon_2^{'}(\lambda)^2 - \varepsilon_2^{'}(\lambda)(\varepsilon_1 + \varepsilon_3) + \varepsilon_1\varepsilon_3 - \varepsilon_2^{"}(\lambda)^2} \right]^{1/3} \tag{27}$$

where λ is the corresponding plasmon resonance wavelength at a given size ratio r_1 / r_2 , and $\varepsilon_2^{'}(\lambda)$ and $\varepsilon_2^{"}(\lambda)$ are the real and imaginary parts of the metallic shell dielectric function.

Figure 5 shows the relation between plasmon resonance wavelength λ and the ratio r_1 / r_2. The blip at $r_1 / r_2 = 0.92$ is caused by the discretization and inaccuracy of experimental dielectric constant data. The ratio of the core radius to the total radius yields a dipolar plasmon resonance peak at a certain frequency. When the ratio increases ($r_2 / (r_2 - r_1) \geq 10$), the corresponding dipolar plasmon resonance

frequency of some dielectric core metal shell nanoparticles will shift into the near-infrared, or even to the infrared.

This study reveals several core-shell particle options have plasmon resonance frequencies in the solar spectrum which can also be red-shifted to the infrared -- a benefit for thermal emission. Further analysis in the Mie scattering regime will be needed for larger size nanoparticles that have larger r_1/r_2 ratios.

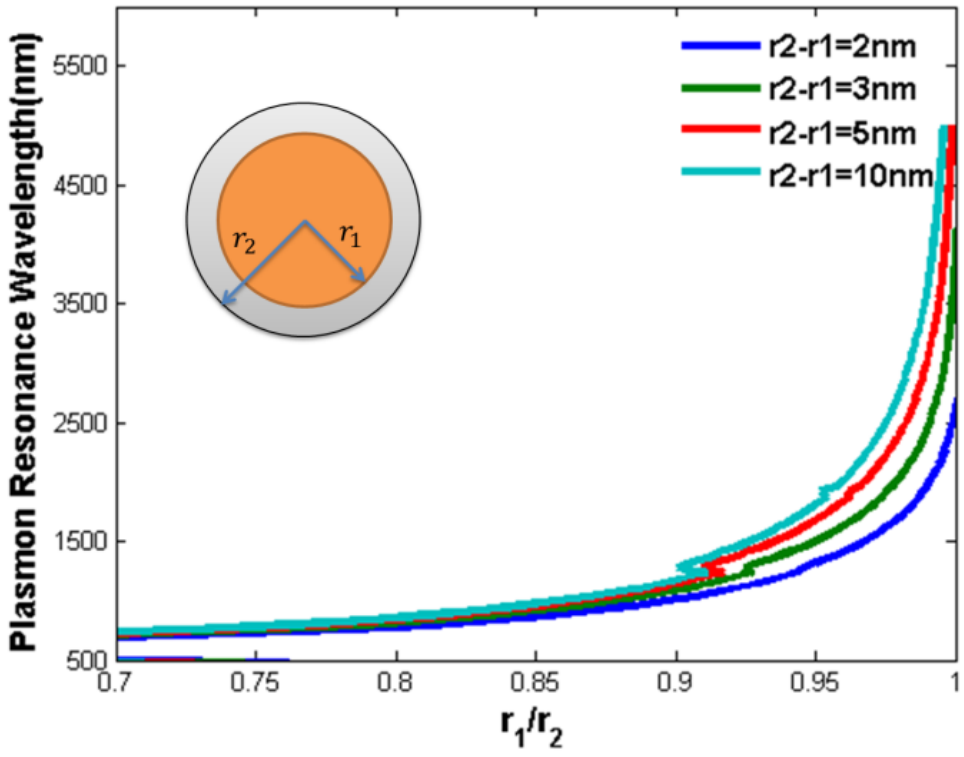

Figure 5 For Si-Au core-shell nanoparticles, prediction of how the plasmon resonance wavelength varies with the ratio of the core radius to the total radius for shell thicknesses r_2-r_1 = 2, 3, 5, 10 nm

ii. Extinction efficiency of Si core and metallic (Au, Ag, Cu, Al) shell nanoparticles (shell thickness $r_2 - r_1$=3nm) suspended in water

Numerical calculations have been done on gold and silver, but aluminum and copper are also included since these materials have greater long-term commercial potential. Table 1 gives the numerical values for the bulk electron mean free path, the bulk plasmon resonance frequency, the free electron Fermi velocity and the tuning range of single particle absorption peak for each material. This information enables the bulk metal free electron scattering time to be calculated by the following equation [76]:

$$\tau_0 = l_\infty / V_f \tag{28}$$

where l_∞ is the bulk free electron mean free path. By inserting τ_0 into equation 24, the effective scattering time τ_{eff} is easily computed.

Table 1 Bulk mean free path of conduction electrons at 273 K, bulk plasma frequency ω_p, and Fermi velocity for potential shell metals [72, 73].

Type	Au	Ag	Cu	Al
Bulk mean free path l_∞ (nm)	42	52	42	16
Bulk plasma frequency $\omega_p(10^{16}\,Hz)$	1.37	1.36	1.64	2.40
Fermi velocity V_f (10^6m/s)	1.38	1.39	1.57	2.03
Tuning range(nm) when r_2-r_1=2nm & r_2 ~6-25nm	700~1200	640~1240	640~1160	440~680

Inserting the bulk plasma frequency w_p, τ_{eff} and experimentally measured dielectric function of the bulk metal allows us to get the dielectric function of the metallic shell by equation 26.

With equations 19-22, the spectral extinction coefficients of core-shell nanoparticle suspensions are able to be computed. Figure 6 shows the calculation of extinction coefficients for Au shell/Si core, Ag shell/Si core, Cu shell/Si core and Al shell/Si core nanoparticle suspensions. As discussed above, Au, Ag and Cu have similar single-particle extinction coefficients when the shell thickness is smaller than the free electron mean free path (list in table 1). The solar irradiation spectrum and the extinction coefficient for pure water are also included. 3 nm

shell thickness is assumed here, since it will have higher extinction coefficient in the solar spectrum. The volume fraction is set at $f_v = 0.05\%$. Note that the y-axis of Fig. 6 is on a logarithmic scale.

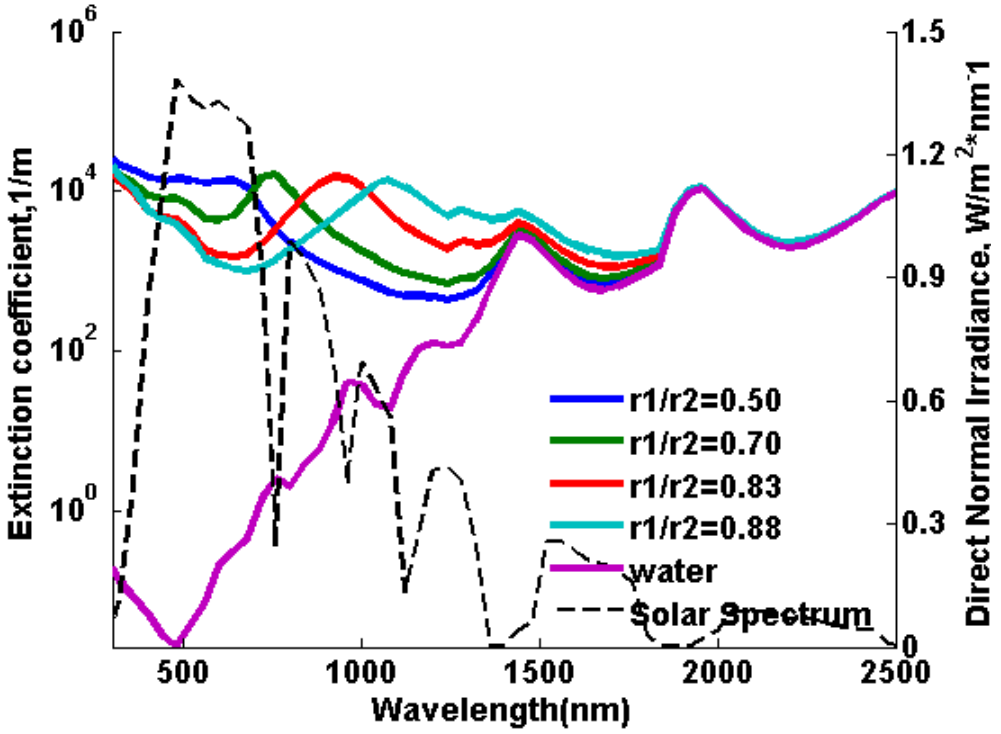

(a)

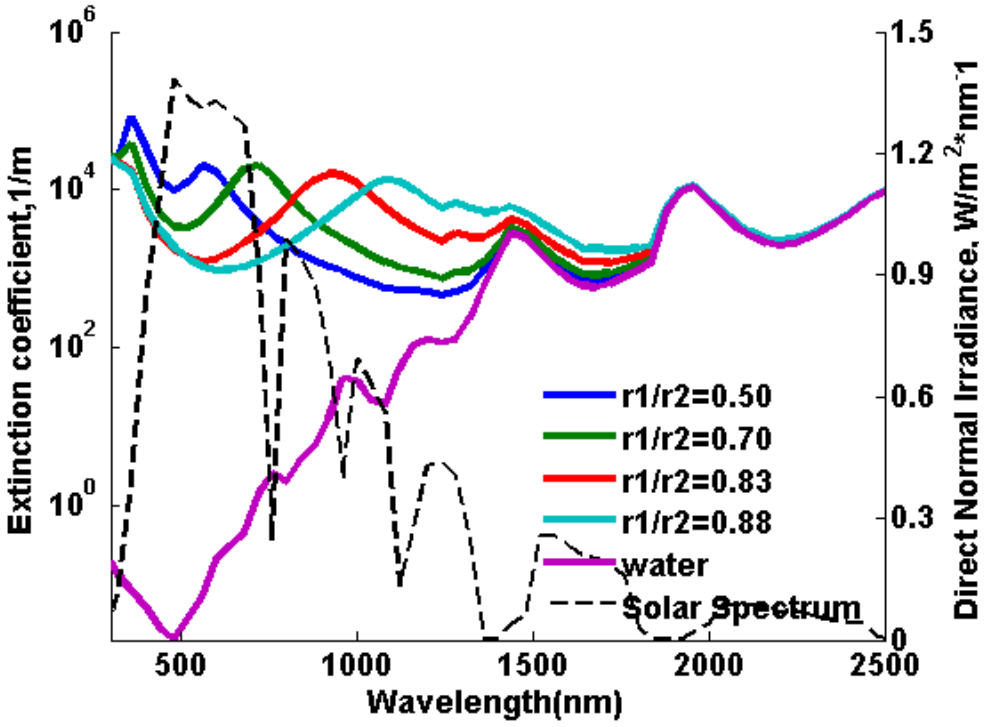
Extinction coefficient,1/m
Direct Normal Irradiance, W/m^2*nm^-1
Wavelength(nm)
r1/r2=0.50
r1/r2=0.70
r1/r2=0.83
r1/r2=0.88
water
Solar Spectrum

(b)

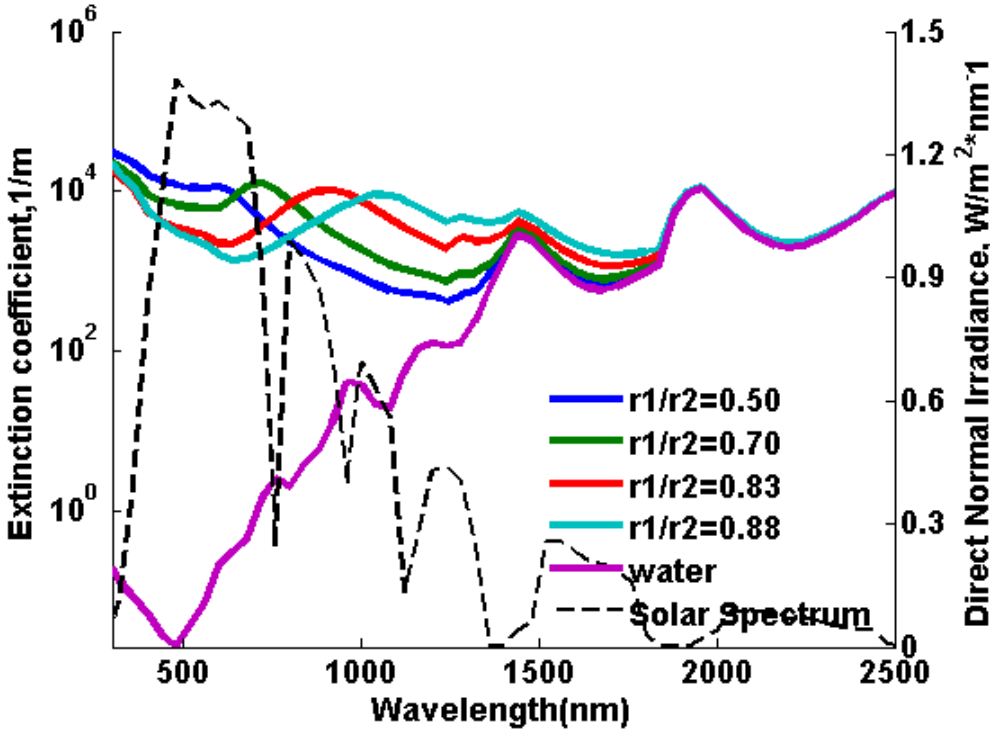
Extinction coefficient,1/m
Direct Normal Irradiance, W/m^2*nm^-1
Wavelength(nm)
r1/r2=0.50
r1/r2=0.70
r1/r2=0.83
r1/r2=0.88
water
Solar Spectrum

(c)

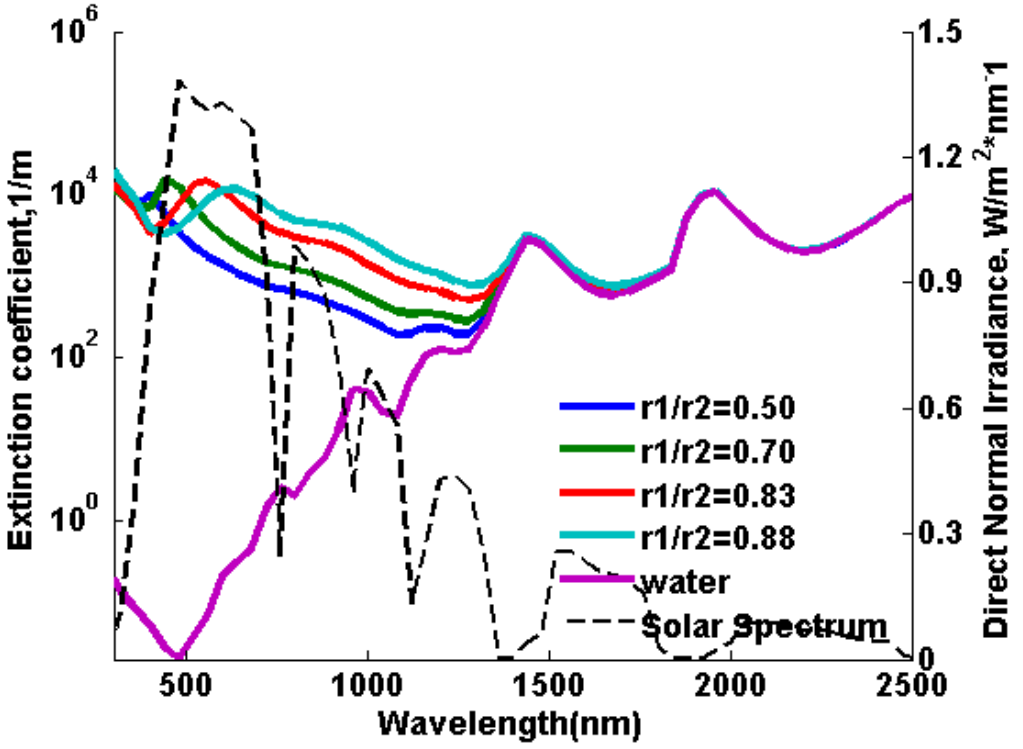

(d)

Figure 6 Extinction coefficients $\sigma_{nanofluid}$ for water-based core shell nanoparticle suspensions (a) Si core/Au shell (b) Si core/Ag shell (c) Si core/Cu shell (d) Si core/Al shell

From Fig. 6, the red-shift of the peak extinction coefficient wavelength as the size ratio increases for all four nanofluids is observed. For comparison, the geometry of the nanoparticles is set to be identical. For silver and copper shell nanoparticle suspensions, they seem to have a similar tuning range as gold, although the bulk optical property is different among gold, silver and copper. In

our case, the effective shell thickness is much smaller than the bulk electron mean free path of the metallic materials. Therefore the dielectric function ε_2 depends on the shell thickness in our example and results in a difference between the bulk and the nanoscale optical response. This explains why Ag and Cu have similar responses to Au. The tuning range of Si-Al core-shell is smaller than that of the other three. The difference can be deduced from Table 1, as the optical properties of bulk Al are much different from the other three. However, the spectral response of Si-Al nanoparticles fits the solar spectrum quite well. It results in a relatively high solar-weighted absorption efficiency of a corresponding nanoparticle suspension.

iii. Solar-weighted efficiency analysis for selecting the best core-shell nanoparticle size and shell thickness.

Figure 6 gives us a visual impression of how a core-shell nanoparticle increases the extinction coefficient of base fluids. The solar-weighted absorption coefficient A_m, which represents the percentage of solar energy absorbed across a fluid layer of selected thickness [80], can be calculated to quantitatively appreciate the escalation:

$$A_m = \frac{\int E_\lambda (1 - e^{-\frac{4\pi k x}{\lambda}}) d\lambda}{\int E_\lambda d\lambda} \tag{29}$$

where E_λ is the solar irradiance per unit wavelength at a certain wavelength, and x is the thickness of the fluid layer, where here we set x = 1.0 cm. The volume fraction is set to be $f_v = 0.005\%$.

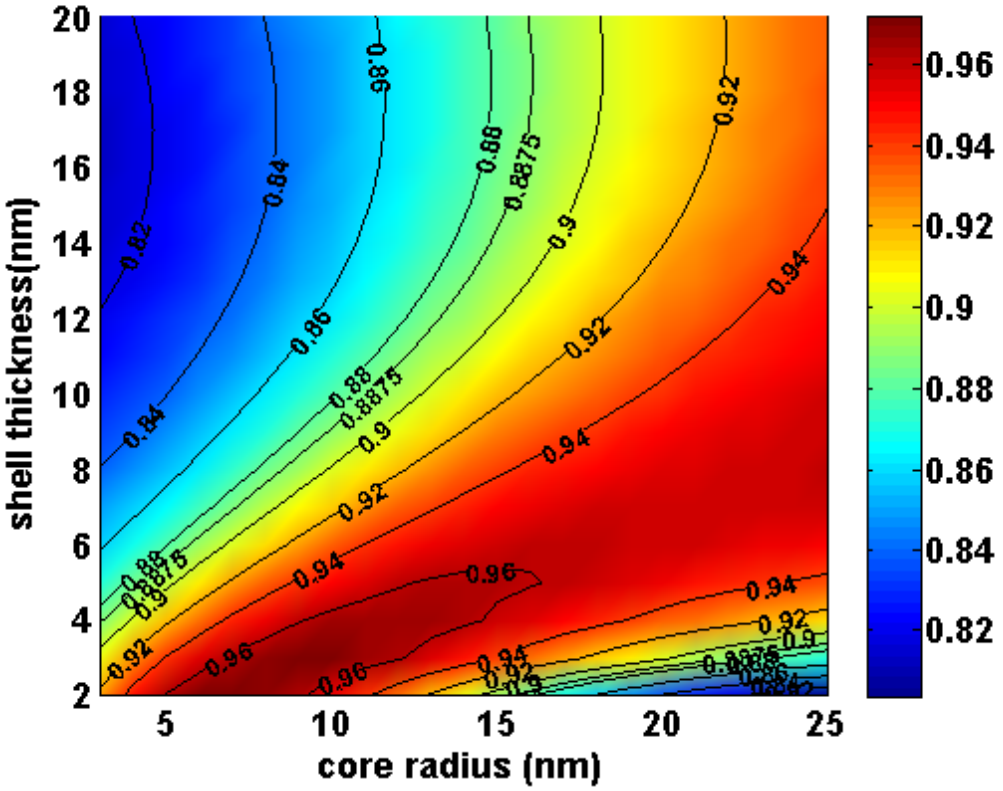

(a)

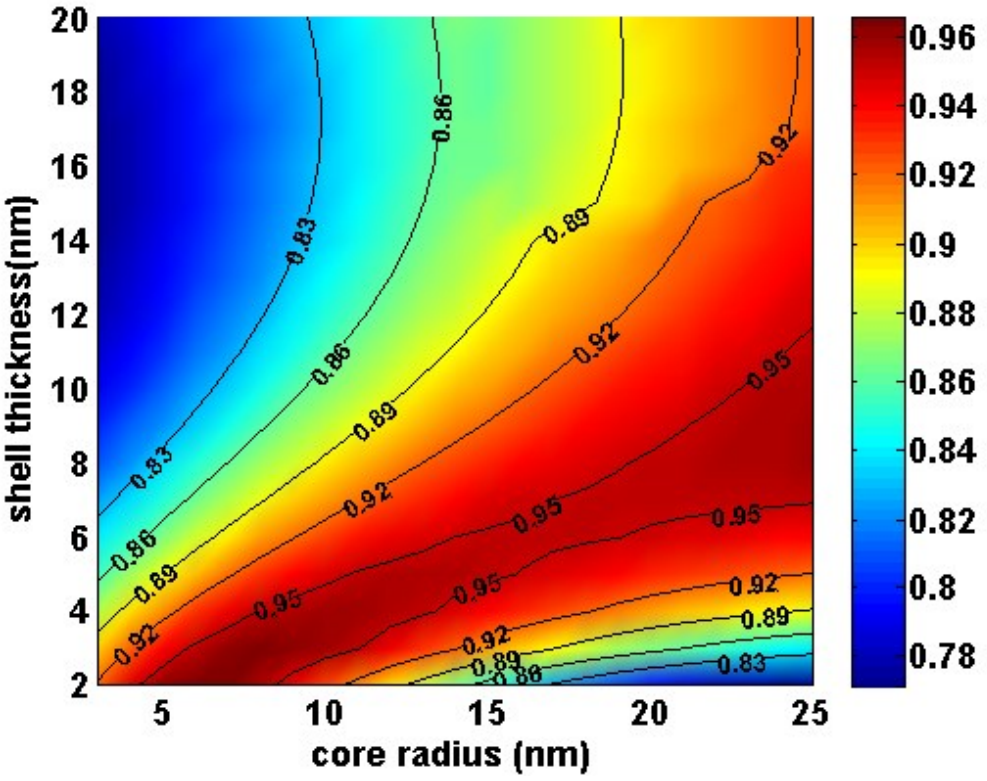
shell thickness(nm)
core radius (nm)
20
18
16
14
12
10
8
6
4
2
5
10
15
20
25
0.96
0.94
0.92
0.9
0.88
0.86
0.84
0.82
0.8
0.78
0.83
0.86
0.89
0.92
0.95

(b)

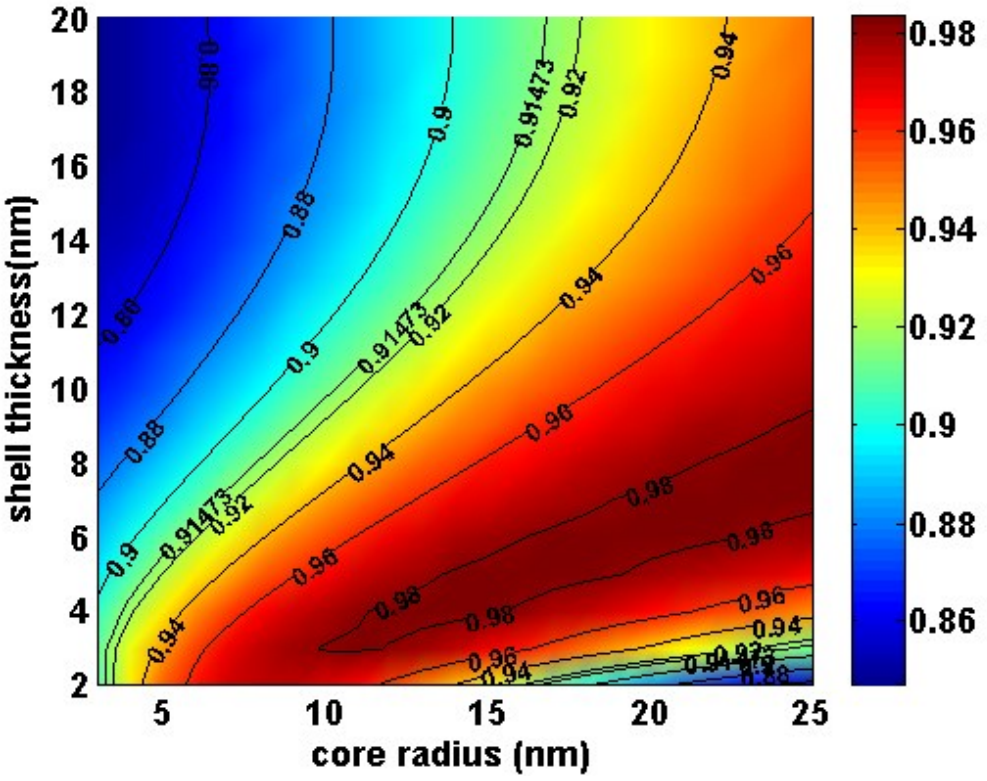
shell thickness(nm)
core radius (nm)
20
18
16
14
12
10
8
6
4
2
5
10
15
20
25
0.98
0.96
0.94
0.92
0.9
0.88
0.86

(c)

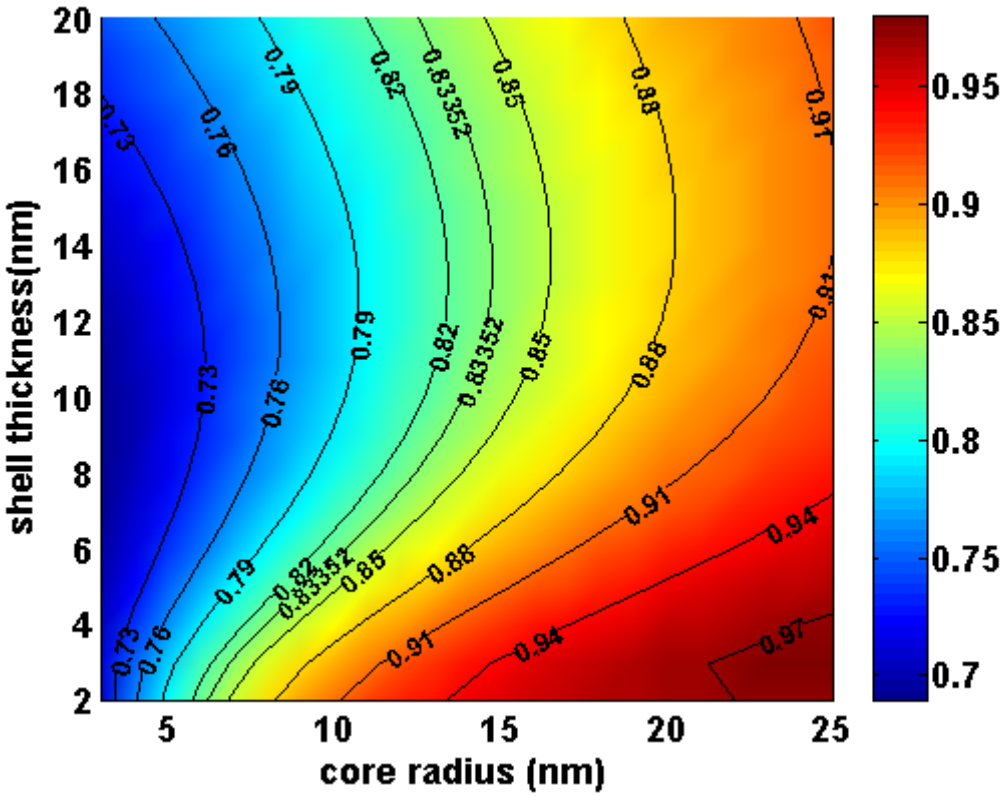

(d)

Figure 7 Contour plot of the solar-weighted absorption A_m for (a) Si core/Au shell (b) Si core/Ag shell (c) Si core/Cu shell (d) Si core/Al shell nanoparticles, with varying core radius (3-25 nm) and shell thickness (2-20 nm)

Figure 7 shows the calculated solar-weighted absorption efficiencies of the nanofluids composed of core-shell nanoparticles dispersed in water. It also shows us the dependence of the core radius and shell thickness on the solar-weighted efficiency or in other words, the solar harvesting capacity for different sizes and shell thicknesses for these kinds of nanofluids. The radiative properties of

dispersions of nanoparticles are highly volume fraction dependent. The nanofluids' solar weighted efficiency still rises significantly compared to that of pure water due to the core-shell nanoparticle's radiative response—a large optical cross section at the corresponding surface plasmon wavelength in the visible region. At certain volume fraction, the optical properties of the nanoparticles then become important. The magnitude of the absorption cross section, the bandwidth of the absorption peak and the location of the absorption peak are important for the solar energy harvesting. Figure 6 provides us an intuitive impression on how the core size and shell thickness impact the core-shell nanoparticle suspensions' solar-weighted efficiency. As discussed above, the optical responses of Au, Ag and Cu nanoparticles are quite similar, which is also reflected in Fig. 7. They all exhibit high solar-energy-harvesting capacity in the region that have certain size ratio to maintain their absorption peaks around 800 nm. Taking Cu as an example, at a core radius r_1=11nm and shell thickness r_2-r_1=3nm, and at a core radius r_1=25nm and shell-thickness r_2-r_1=8nm, the same solar-weighted efficiency A_m=0.9829 is obtained. As for Al, consistent with the spectra plot Fig. 6(d), its absorption peak matches the solar spectrum even at large size ratio (r_1/ r_2). The best solar-weighted efficiency for Si/Al core shell nanoparticles occurs at large size ratios. Table 2 lists the best solar-weighted efficiency and corresponding geometry of these four different core-shell nanoparticle suspensions. Note: for Cu,

it has the exact same highest solar-weighted efficiency at two different geometries.

Table 2 Solar weighted absorption coefficient (AM1.5 λ 0.3-2.6 um x=1.0cm).

Type	Au	Ag	Cu_1	Cu_2	Al
Core radius (nm)	7	6	11	25	25
Shell-thickness (nm)	2	2	3	8	3
Solar-weighted efficiency	0.9714	0.9655	0.9829	0.9829	0.9788
SPR Wavelength (nm)	800	760	800	840	640
C_{sca} / C_{abs} at SPR	3.3E-5	6.4E-5	8.2E-4	0.016	0.012

Table 3 gives plank-weighted emittance efficiency of different nanofluids. The spectrum ranges from 0.2 um to 9.54um. It is computed by equation 29 with blackbody radiation spectrum at different temperature instead of solar spectrum. From table 3, it can tell that the emittance efficiency of nanofluids is very high due to the good emittance at IR spectrum of base fluid (water). At low temperature (200C), it is identically to 1. And at high temperature (800C), there are small variances between different nanofluids.

Table 3 Plank-weighted emittance efficiency of core-shell nanoparticle suspensions at different temperature

Shell-Type (wavelength)	Au(0.2~9.56um)	Ag(0.2~9.52um)	Cu(0.2~9.52um)	Al(0.2~9.52um)
Planck-weighted emittance @ 200 C r_1=2nm;r_2(6~25nm)	1.00	1.00	1.00	1.00
Planck-weighted emittance @ 800 C r_1=2nm;r_2=6nm	0.9978	0.9978	0.9976	0.9964
Planck-weighted emittance @ 800 C r_1=2nm;r_2=10nm	0.9990	0.9991	0.9987	0.9970
Planck-weighted emittance @ 800 C r_1=2nm;r_2=18nm	0.9999	0.9999	0.9998	0.9981
Planck-weighted emittance @ 800 C r_1=2nm;r_2=25nm	0.9998	0.9998	0.9998	0.9989

8) Conclusions

The radiative and optical responses of a dispersion of silicon/metallic core shell nanoparticles were modeled and compared under several approximations. The motivation of this study is to find nanofluids whose radiative properties can be controlled. Under quasi-static and Rayleigh scattering approximations, the silicon/metal core shell nanoparticle exhibits a reasonable tuning range of its dipolar surface plasmon resonance frequency. Analysis of the extinction

coefficient of four different dielectric core/metallic shell core-shell nanoparticle suspensions and their corresponding solar-weighted efficiency reveals their alterable optical responses and potential for solar energy harvesting. One key conclusion is that core-shell nanoparticles provide the same solar-weighted absorption efficiency in comparison to pure metal nanoparticles with less volume fraction of metal. Taking an 18-nm-radius Au nanoparticle as an example, the same size Si-Au core shell nanoparticle (2 nm shell thickness) will only need 30% Au by volume, compared with a corresponding solid nanoparticle. Another essential conclusion is that Aluminum and Copper core-shell nanoparticle suspensions can have equivalent or better solar-weighted efficiencies than noble metal core-shell nanoparticle suspensions.

1) Introduction

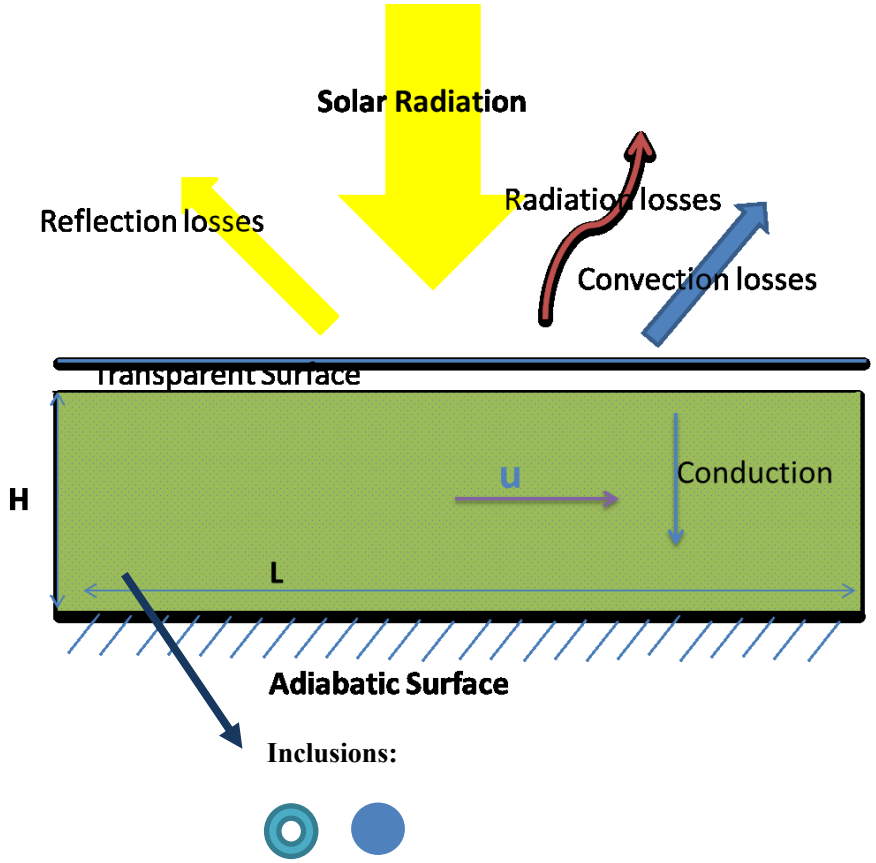

Figure 8 Direct absorption solar collector using core shell multifunctional nanoparticles and solid nanoparticles.

This chapter emphasizes the surface plasmon effect in application to direct solar absorption collectors (DAC). As mentioned above, solar thermal collectors using dispersions of small particles acting as direct solar collectors have been studied in recent years [53,81]. Unlike conventional surface absorbing solar

thermal collectors, direct absorption is a volumetric approach which has several advantages. The absorption efficiency of incoming sunlight in a highly absorbing particles-embedded media goes beyond that of surface absorption of a similar material. Secondly, the overall thermal resistance can be reduced by reducing the need for convection and conduction heat transfer between the absorbing surface and the working fluid [49]. The optical properties of nanoparticle suspensions (nanofluids) could have dramatic impacts on the absorption and emission of DAC energy systems. The spectral properties of a system are of great importance for a well-designed system whose main thermal transport process is radiation. In this chapter, the author researches potential nanostructures and compares the optical properties of graphite, metallic nanospheres and core-shell nanoparticles-based water suspensions. Next, a solar-weighted efficiency table is presented. Lastly, a two-dimensional volumetric absorption model is used to calculate the overall system efficiency of different nanostructures-laden nanofluids-based DAC.

Figure 8 shows the basic scheme of the direct absorption system. The top part is a glass sheet which reduces the infrared thermal emission. The major part of solar energy is absorbed in the liquid film which contains different kinds of heat transfer fluid (water, therminol VP-1, ionic liquid) laden by nanoscale structures. Only water is considered as basefluid here for simplicity. There are three groups

of nanoscale particles discussed here which are solid metallic and graphite nanospheres, and core-shell nanoparticles made of metal shell with Si core.

2) Optical Properties Comparison between Solid Nanoparticle and Core-Shell Nanoparticle Suspensions

Figure 8 contains the basic geometric scheme of a volumetric DAC containing either core-shell nanoparticles or solid metallic nanospheres. In this work, the core of the core-shell nanoparticles is made of dielectric material (silicon), and the shell and solid nanospheres can be made of metallic materials (Ag, Au, Al, Cu and Ni). Due to the SRP effect, different materials have different peak absorption frequencies. The core-shell nanoparticles' SPR frequency depends also on particle size, shape, shell thickness and dielectric properties of the core and surrounding media. In our application, investigating materials which have the best solar energy harvesting capability is necessary. For economic considerations, relatively low-cost graphite nanoparticles are also considered.

First of all, the radiative properties of solid metallic nanoparticles and graphite nanoparticles are required to be computed. Analogous to the core-shell nanoparticles modeling, nanoparticle size is limited to the Rayleigh regime. Commonly available nanoparticles in solar nanofluids [37] are in the range of 5-50 nm average particle diameters, for which most of the incident light from the

sun has a wavelength that is at least 10 times larger. There are two major reasons for choosing this small size of nanoparticles. When the nanoparticle diameter is much smaller than the wavelength of the incident field, higher order terms in the Mie scattering solution are negligible and the approximation of Rayleigh scattering ($\pi \mathrm{D} / \lambda << 1$) is applicable. In this work, the size of the nanoparticles is limited to those smaller than 50 nm.

The absorption, scattering, and extinction efficiencies for solid metallic and graphite nanoparticles can be calculated by the following equations, which can be found in several standard texts such as Bohren and Huffman [27]:

$$Q_{sca} = \frac{8}{3}\alpha^4 \left| \frac{m^2 - 1}{m^2 + 2} \right|^2 \tag{30}$$

$$Q_{abs} = 4\alpha \left\{ \frac{m^2 - 1}{m^2 + 2} \left[1 + \frac{\alpha^2}{15} \left(\frac{m^2 - 1}{m^2 + 2} \right) \frac{m^4 + 27m^2 + 38}{2m^2 + 3} \right] \right\} \tag{31}$$

$$Q_{ext} = Q_{abs} + Q_{sca} \tag{32}$$

where m is the relative complex refractive index of the nanofluid (divided by the real part of the refractive index of the fluid), α the size parameter, which is defined as [27] $\pi \mathrm{D} / \lambda$, D the nanoparticle diameter, and λ the incident wavelength. Note that for materials which are optically anisotropic (e.g. graphite),

the absorption, scattering, extinction efficiency is the average of the parallel and perpendicular graphite planes.

For nanoscale metallic and graphite nanoparticles with very small size parameters, the scattering efficiency is much smaller than the absorption efficiency owing to Q_{sca} being proportional to α^4. If it is negligible, the scattering efficiency simply drops out of the nanoparticles' extinction coefficient equation [29]:

$$\sigma_{particle} = \frac{3 f_v Q_{ext}}{2D} = \frac{3 f_v Q_{abs}}{2D} \tag{33}$$

where $\sigma_{particle}$ is the effective nanoparticles' extinction coefficient in the nanofluid.

In order to calculate the absorption and scattering cross sections of nanoparticles, the dielectric function of metallic nanostructures is needed. For graphite nanoparticles, the calculation is straightforward. Taking the parallel and perpendicular grains refractive index into equations 30-33, one can get the effective extinction efficiency from the average of the two planes. As for metal and core-shell nanoparticles, modifications are needed to calculate the effective dielectric function of metallic components since the electron mean free path is close to or even bigger than the particle size. Optical properties of the bulk metallic material are acquired from Palik [76]. When the dimension of the nanostructures decreases below the mean free path of the bulk material the

interaction of the oscillation with the boundary increases, hence the optical properties need to be adjusted. Readers are recommended to read the previous chapter on the Drude-Lorentz model & the size effect.

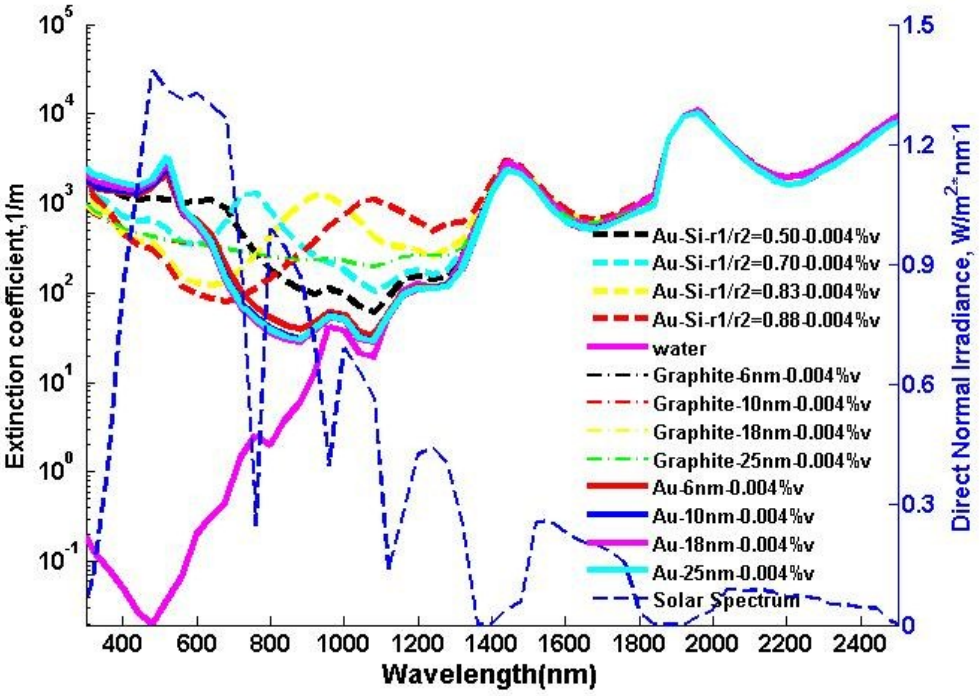

(a)

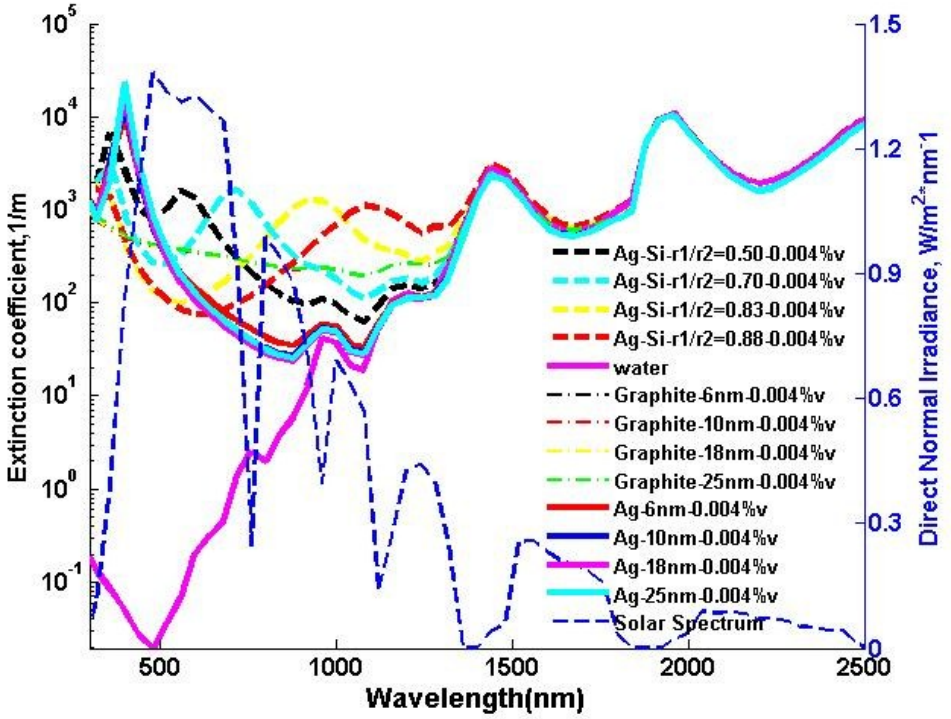
Extinction coefficient,1/m
Direct Normal Irradiance, W/m2-nm-1
Wavelength(nm)
Ag-Si-r1/r2=0.50-0.004%v
Ag-Si-r1/r2=0.70-0.004%v
Ag-Si-r1/r2=0.83-0.004%v
Ag-Si-r1/r2=0.88-0.004%v
water
Graphite-6nm-0.004%v
Graphite-10nm-0.004%v
Graphite-18nm-0.004%v
Graphite-25nm-0.004%v
Ag-6nm-0.004%v
Ag-10nm-0.004%v
Ag-18nm-0.004%v
Ag-25nm-0.004%v
Solar Spectrum

(b)

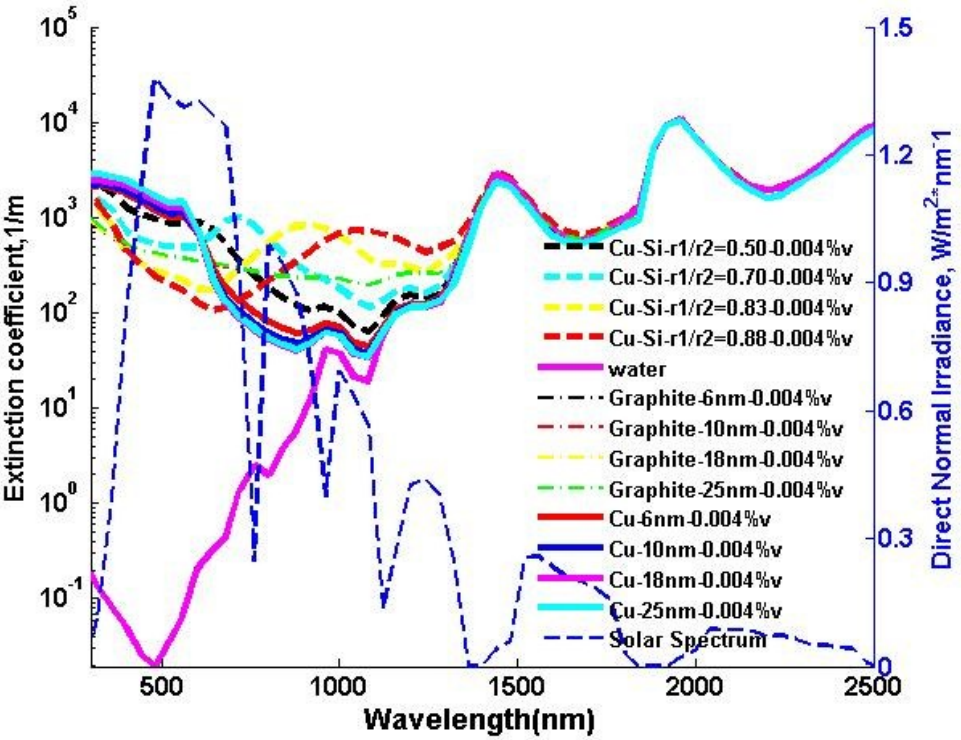
Extinction coefficient,1/m
Direct Normal Irradiance, W/m2-nm-1
Wavelength(nm)
Cu-Si-r1/r2=0.50-0.004%v
Cu-Si-r1/r2=0.70-0.004%v
Cu-Si-r1/r2=0.83-0.004%v
Cu-Si-r1/r2=0.88-0.004%v
water
Graphite-6nm-0.004%v
Graphite-10nm-0.004%v
Graphite-18nm-0.004%v
Graphite-25nm-0.004%v
Cu-6nm-0.004%v
Cu-10nm-0.004%v
Cu-18nm-0.004%v
Cu-25nm-0.004%v
Solar Spectrum

(c)

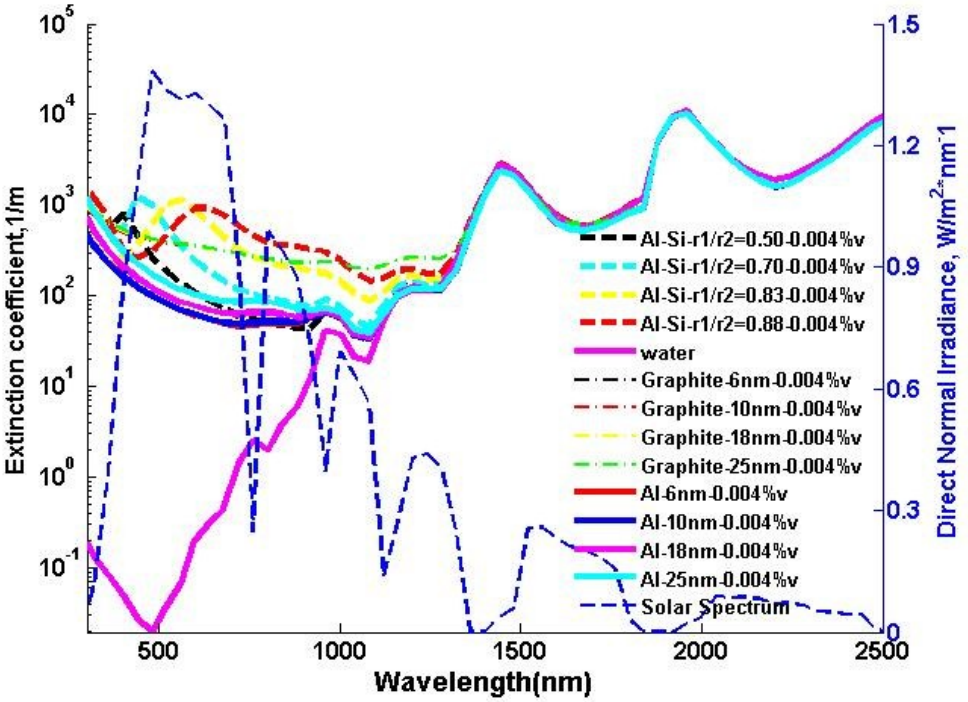
Extinction coefficient,1/m
Direct Normal Irradiance, W/m2*nm-1
Wavelength(nm)
Al-Si-r1/r2=0.50-0.004%v
Al-Si-r1/r2=0.70-0.004%v
Al-Si-r1/r2=0.83-0.004%v
Al-Si-r1/r2=0.88-0.004%v
water
Graphite-6nm-0.004%v
Graphite-10nm-0.004%v
Graphite-18nm-0.004%v
Graphite-25nm-0.004%v
Al-6nm-0.004%v
Al-10nm-0.004%v
Al-18nm-0.004%v
Al-25nm-0.004%v
Solar Spectrum

(d)

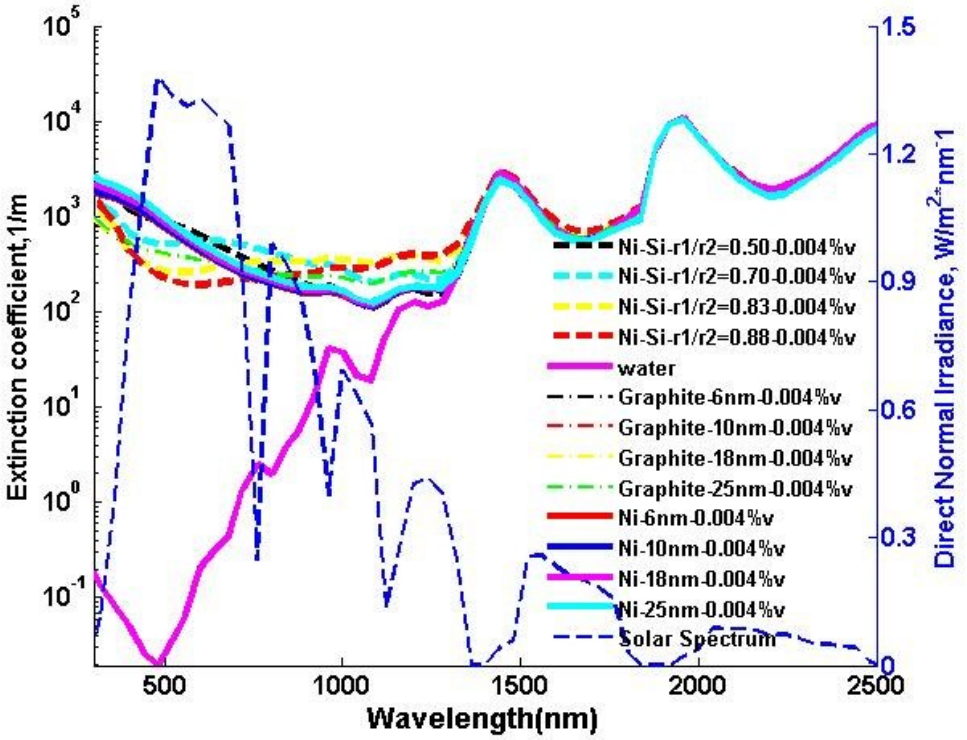

(e)

Figure 9 Extinction coefficients of graphite, solid metal nanoparticles, and core-shell nanoparticles at different size (the shell thickness of core-shell NPs is 3nm, volume faction 0.004%)

Figure 9 shows the computational results of the optical properties of several nanofluids. These metal materials are chosen for comparison since they have been considered for direct solar absorption collector application. The inclusions in the fluid are different sizes of graphite, solid metal nanoparticles and corresponding core-shell nanoparticles. For graphite nanoparticles, which are the green chain dotted line in figure 9, different size graphite nanoparticles-laden nanofluids have

identical spectral extinction coefficient as they overlap on one line. As for solid metal NPs, some exhibit a surface plasmon effect which can be observed by the absorption peak at a plasmon resonance frequency, like Au, Ag, and Cu. A 'small' variance between different sizes of solid metallic nanoparticles can be observed. As for core-shell nanoparticles, the ratio effect (ratio between the core and total radius r_1/r_2) is obvious. The extinction peaks rise for most metallic shell Si core nanoparticles except Ni. What's more, the surface plasmon resonance frequency can be tuned to longer wavelengths by adjusting the core-shell ratio and material intrinsic optical properties. The full width at half maximum (FWHM) extinction coefficients of core-shell nanoparticles-laden nanofluids is larger than the corresponding solid metallic nanoparticles suspensions. All these calculated optical responses indicate that the metallic shell dielectric core nanoparticles-laden fluids can serve as promising candidates for direct absorption solar collectors, which require great light concentrating and absorption ability in the solar spectrum. Note the shell thickness of core-shell nanoparticles is 3 nm. The two peaks around 1.5 μm and 2 μm are caused by the water that is a much stronger absorber in the infrared spectrum than the nano-composites used in the study.

Each nanofluid's solar-weighted absorption efficiency at a volume faction of 0.004% is listed in Table 4 for all nanofluids considered here. And the metallic shell thickness is still kept at 3nm for core-shell nanoparticles.

Table 4 Solar weighted absorption efficiency (AM1.5, $\lambda = 280 - 2500(nm)$, x=1.0cm).

0.008% vf	**0.004% vf**	**0.004% vf**	
Au-Si core shell NPs (3nm shell)		Au NPs	**Particle Size**
0.9397	0.8821	0.761	**6nm**
0.9199	0.8862	0.7361	**10nm**
0.917	0.8476	0.7236	**18nm**
0.8856	0.7844	0.7309	**25nm**
Ag-Si core shell NPs (3nm shell)		Ag NPs	
0.9386	0.8754	0.6818	**6nm**
0.9212	0.8807	0.6417	**10nm**
0.9017	0.8099	0.6278	**18nm**
0.8651	0.7428	0.6489	**25nm**
Cu-Si core shell NPs (3nm shell)		Cu NPs	
0.9438	0.8855	0.7983	**6nm**
0.9221	0.8916	0.7659	**10nm**
0.9312	0.882	0.7458	**18nm**
0.9119	0.8274	0.7502	**25nm**
Al-Si core shell NPs (3nm shell)		Al NPs	
0.7908	0.6584	0.554	**6nm**
0.8336	0.7346	0.5523	**10nm**
0.9088	0.8592	0.6033	**18nm**
0.9273	0.8958	0.676	**25nm**
Ni-Si core shell NPs (3nm shell)		Ni NPs	
	0.9332	0.9114	**6nm**
	0.9129	0.9142	**10nm**
	0.8982	0.9216	**18nm**
	0.8586	0.9302	**25nm**
		Graphite NPs	
		0.9493	**6nm**
		0.9494	**10nm**
		0.9498	**18nm**
		0.9506	**25nm**

From figure 9, a noticeable surface plasmon effect on solid Au, Ag and Cu nanoparticles and Au, Ag, Cu, Al core Si shell nanoparticles is observed. The SPR effect on metallic nanostructures can largely enhance the absorption and scattering ability of the nano-composites at the plasmon resonance frequency, which is reflected as an extinction coefficient peak in the extinction spectrum. Consistent with figure 9, the plasmatic metallic materials in core-shell form exhibits greater solar-weighted efficiency than in solid nanosphere form since the FWHM of the peak extinction coefficients become broader. Some core-shell nanoparticles' plasmon resonance frequency matches the solar spectrum quite well.

For Ni and Graphite, the corresponding solid nanoparticles demonstrate good solar absorption ability. Although they do not show strong surface plasmon effect, they still can serve as decent and cost-effective materials for direct solar absorption nanofluids.

However， as for plasmonic nanostructures suspensions, there is a possibility that the simple adding method under-predicts the extinction coefficient of the mixtures. One of the coauthors has studied the effective extinction coefficient of nanoparticle suspensions via different methods including Maxwell-Garnet theory and the simple adding method used here[37]. When compared to the experimental results, both of them underpredict the plasmatic nanoparticles suspension,

although the latter one works better. Future work will be needed to precisely predict the effective extinction coefficient of the mixture. It is beyond the scope of our discussion here. The reader is recommended to Refs. [37,82] for details regarding the Maxwell-Garnet theory and one-dimensional adding method for nanofluids extinction coefficient modeling.

The last column in table 4 is listed for higher loading, core-shell nanoparticles-based nanofluids. The core-shell structure makes it possible to dynamically control the size of nanoparticles by changing the environmental properties like temperature, pH or magnetic field. One possible way, as demonstrated by Ma et al. [83], is by adding temperature-sensitive gel in the core so that the size of the core-shell nanoparticles can be controlled. Assuming 0.004% volume percentage 20-nm radii core-shell nanoparticles are selected initially, by expanding 25% of the initial radius, the volume percentage increases to 0.0078% which has a strong effect on the mixture's optical properties as presented in column 3 of table 4.

3) Volumetric Absorption Solar Collector Model & Results

After the radiative properties are calculated, a numerical model is needed for prediction of direct solar absorption collector efficiency. The structure of the solar collector is illustrated in figure 8. The incoming solar energy enters the top thin

glass, and is volumetrically absorbed in the liquid film. Most of the solar energy is captured by the nanoparticles due to their large surface area and light concentrating ability. They convert the photon energy into phonons and then the thermal energy diffuses to the liquid medium. There are also reflection, convection and radiation losses though the boundaries.

The simplified radiative transport equation for a one-dimensional medium, which neglects the in-scattering term, is expressed as:

$$\frac{dI_{i,\lambda}}{dy} = \sigma_{\alpha,\lambda} I_{b,\lambda}(T(y)) - \sigma_{e,\lambda} I_{i,\lambda} \tag{34}$$

where $\sigma_{\alpha,\lambda}$ and $\sigma_{e,\lambda}$ are the spectral absorption and extinction coefficients, I the intensity, and $I_{b,\lambda}$ the spectral blackbody intensity. The in-scattering term is neglected here since when the size of the particle is in the Rayleigh regime (r<=25 nm), the scattering efficiency is trivial comparing to the absorption efficiency. This approximation is made for solid nanoparticles [49] and core-shell nanoparticles in the Rayleigh regime [79]. The subscript *i* is used to characterize the direction of the light propagation, (+1) for incoming and (-1) for outgoing light. The boundary conditions are specified by Kumar and Tien [53] as

$$I_{-1,\lambda}(L) = \varepsilon_{w,\lambda} I_{b,\lambda}(T(L)) + \rho_{w,\lambda} I_{+,\lambda} \tag{35}$$

$$I_{+1,\lambda}(0) = S_\lambda(1-\rho_{g,\lambda}-\alpha_{g,\lambda}) + \rho_{g,\lambda} I_{-1,\lambda}(0) + \alpha_{g,\lambda} I_{b,\lambda}\left(T(0)\right) \tag{36}$$

where L represents the bottom of the solar collector, $\varepsilon_{w,\lambda}$ the spectral wall emittance, $\rho_{w,\lambda}$ $\rho_{g,\lambda}$ the spectral reflectance of the wall and glass, $\alpha_{g,\lambda}$ the spectral glass absorptance, and S_λ the spectral radiation incident on the receiver. Blackbody radiation is assumed for the spectral properties of the incoming light and emitted radiation:

$$I_\lambda(T) = \frac{2n^2 hc_0^2}{\lambda^5\left[\exp(\frac{hc_0}{\lambda k_B T})-1\right]} \tag{37}$$

where n is the effective real part of the refractive index of the medium, h Planck's constant, k_B the Boltzmann constant, and c_0 the speed of light in vacuum. The above equations are coupled with the 2D energy equation with specified boundary conditions,

$$k\frac{\partial^2 T}{\partial y^2} - \frac{\partial q_r}{\partial y} = \rho c_p U \frac{\partial T}{\partial x} \tag{38}$$

x=0, 0<y<L, $T(0,y) = T_{inlet}$

y=L, x>0, $q_r(L) - k\frac{\partial T}{\partial y}\Big|_{y=L} = 0$

$y = 0$, $x>$ 0, $h\left[T_\infty - (T\ x)\right]0 = -\ k\frac{\partial T(x,\ y)}{\partial y}\Big|_{y=0}$

where k, ρ, c_p, and U are the thermal conductivity of the fluid, density, specific heat, and velocity, respectively. T is the temperature and q_r is the radiative heat

flux. The combined convection and radiative energy loss coefficient h on the top surface is assumed to be 24 W $m^{-2}K^{-1}$ which is derived from experimental data [49] and the bottom is set to be perfect insulation and no heat loss. And last but not least, the receiver efficiency is defined as [29]:

$$\eta = \frac{\dot{m} c_p (T_{out} - T_{in})}{G A_R} \tag{39}$$

where $\dot{m}$, c_p, T_{out}, T_{in}, G, A_R are the mass flow rate, specific heat of fluid, the outlet temperature, the inlet temperature, the solar flux incident, and the collector area respectively. The reader is recommended to find more details from the coauthors' work [49,51,54]. In order to get the best efficiency, the back surface is set to be a perfect reflector. The following parameters are assumed for all cases: G=1000 W/m^2, film thickness H=0.01m, receiver length L=1m, receiver width W=1m, $\dot{m}$=7.2 kg/s, the initial condition T_{in}=323.15(K), ambient temperature T_{amb} = 308.15 (K) and the volume faction is 0.05%. The geometric quantities are chosen for non-dimensionless analysis. The initial and boundary conditions are picked by previous experimental conditions[49]. The flow rate is chosen for higher efficiency and less calculation time. Note the initial condition and the environmental conditions will have an effect on the final efficiency. These specified conditions are maintained constant here in order to simplify comparisons. In order to compare the efficiency of solid metallic nanoparticles

and core-shell nanofluids-based direct solar absorption collector, Au and Al are chosen, as the metallic components of these two nanostructures.

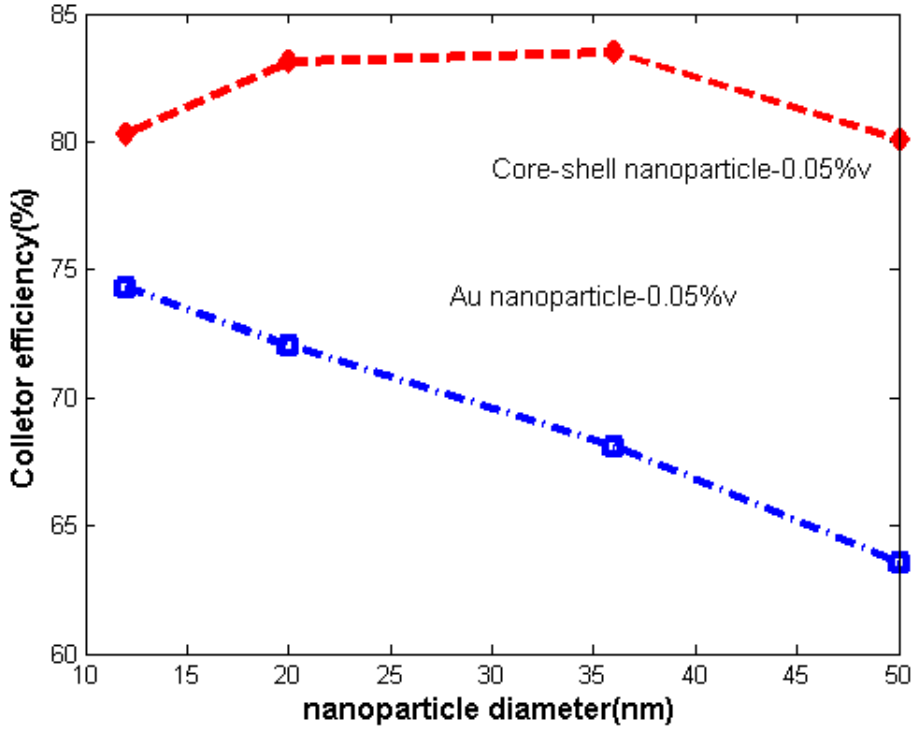

(a)

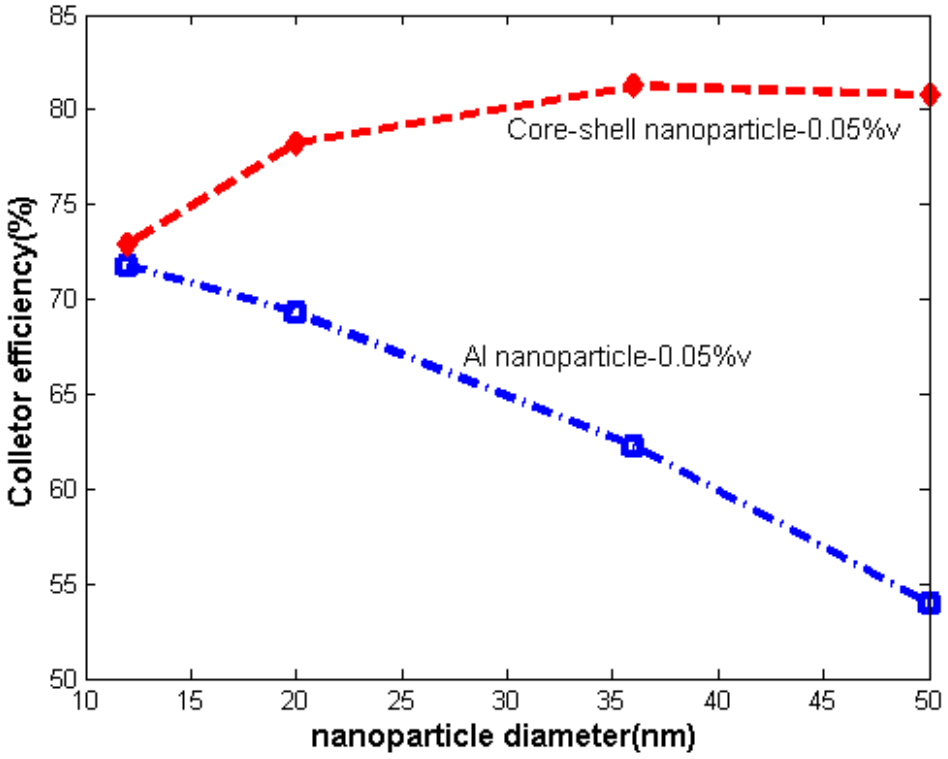

(b)

Figure 10 The collector efficiency of metallic nanoparticles and core-shell nanoparticles based DAC system (volume faction is 0.05%)

From figure 10, the trend of collector efficiency varying with the particle size or aspect ratio (core-shell ratio) is displayed. First of all, the core-shell nanoparticles have better efficiency than solid ones. Secondly, the efficiency decreases as the size of the solid metallic nanoparticles increases. Thirdly, the efficiency of core-shell nanoparticle suspensions first increases, reaches a maximum, then decreases. The tuning of the plasmon resonance frequency causes it. The SPR frequency right-shift to longer wavelengths fits the solar spectrum at

the beginning, and then drops when the SPR wavelength tunes to the near-infrared or infrared region.

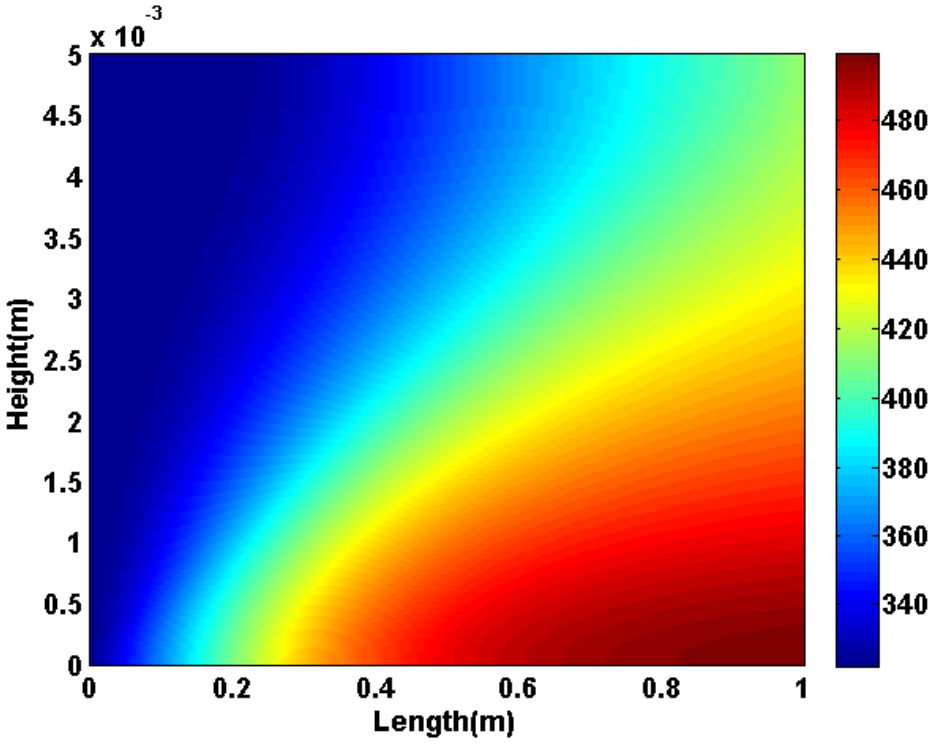

(a)

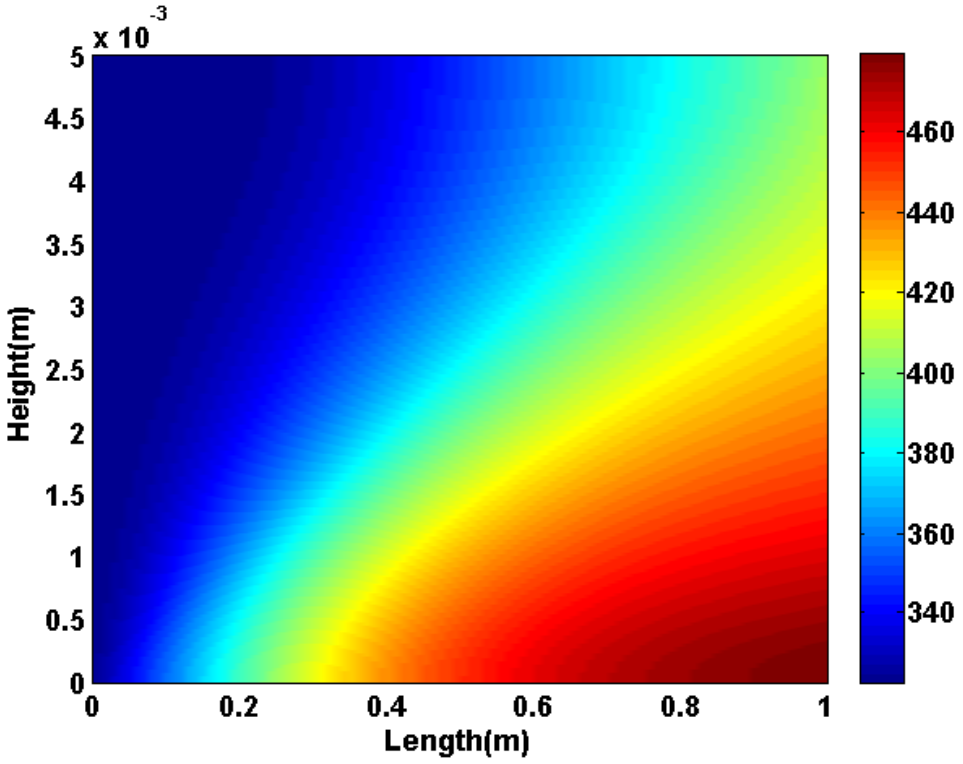
x 10^-3
5
4.5
4
3.5
3
2.5
2
1.5
1
0.5
0
Height(m)
0
0.2
0.4
0.6
0.8
1
Length(m)
460
440
420
400
380
360
340

(b)

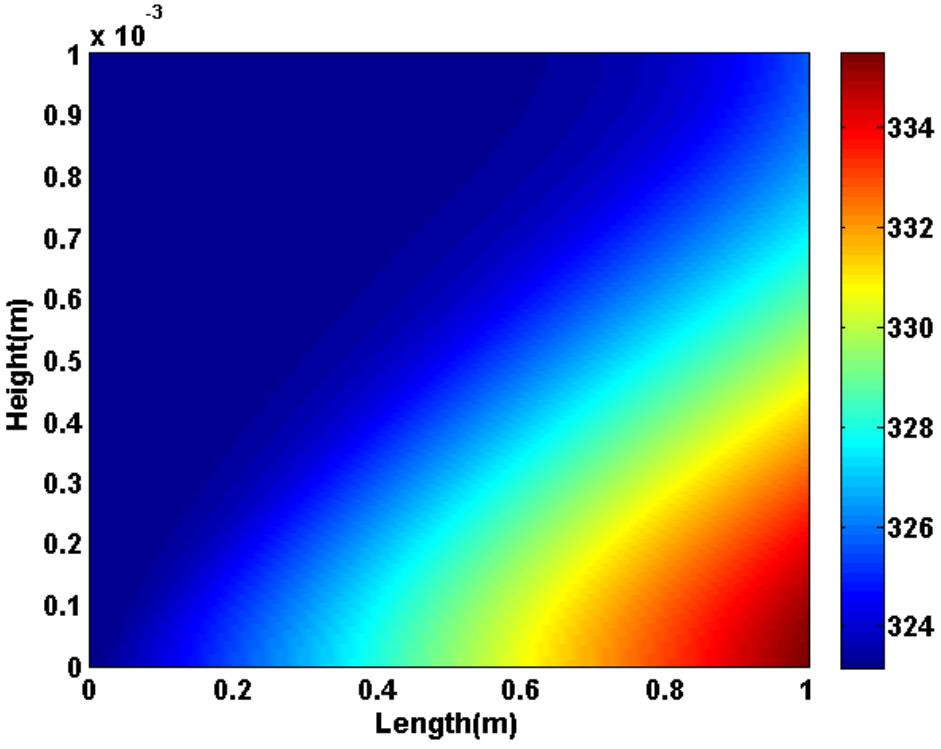
x 10^-3
1
0.9
0.8
0.7
0.6
0.5
0.4
0.3
0.2
0.1
0
Height(m)
0
0.2
0.4
0.6
0.8
1
Length(m)
334
332
330
328
326
324

(c)

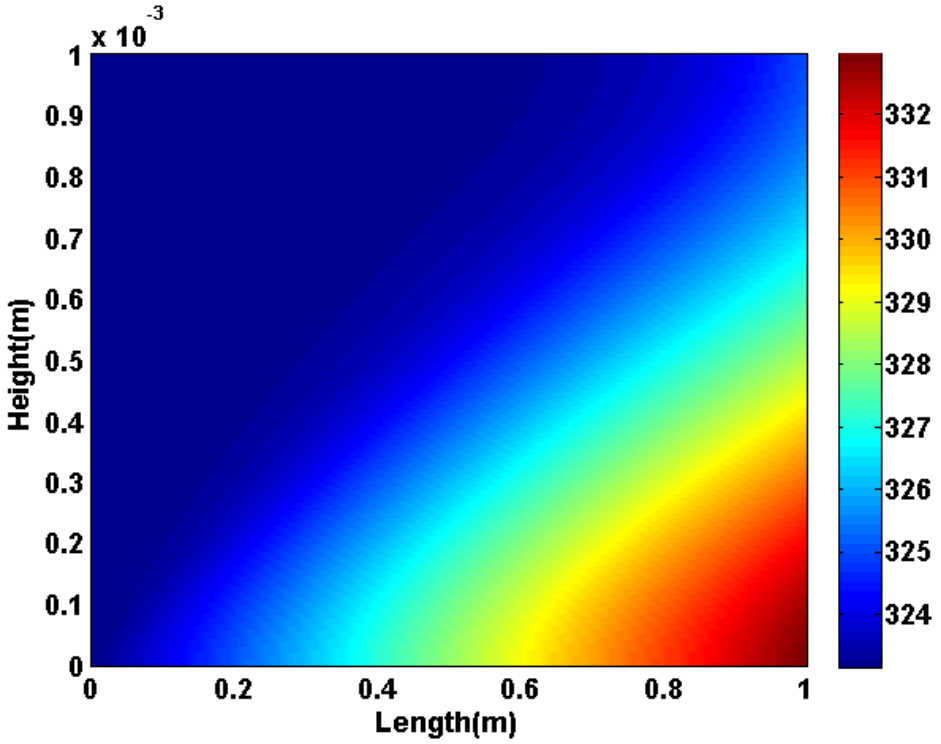

(d)

Figure 11 Temperature field (a) Al (r=6nm) nanofluids mass flow rate at 0.05kg/s; (b) Al (r=25nm) nanofluids mass flow rate at 0.05kg/s; (c) Al (r=6nm) nanofluids mass flow rate at 1kg/s; (d) Al (r=25nm) nanofluids mass flow rate at 1kg/s.

Figure 11 gives the temperature field of the nanofluid. The mass flow rate is set to be lower than that mentioned above, and the height of the fluid set to be lower than before in order to see the temperature field more clearly. (Note: the collector efficiency will be dramatically reduced). It is possible to extrapolate the temperature fields from former case, however the temperature differences are

focused on a very thin layer on the top of the fluid film due to the high mass flow rate. The efficiency difference for different size of nanoparticle suspensions exist, and is around 10% between 6nm (radius) Al nanofluids and 25nm (radius) Al nanofluids at both flow rates. From figure 11, the highest temperature difference ((a) & (b), (c) & (d)) can be observed at two different flow rate conditions. The efficiency difference for the size variation of nanofluids should be caused by this highest temperature difference. The smaller particle size leads to higher outlet fluid temperatures, which leads to higher efficiency of small size nanoparticle-suspension-based solar collectors.

CHAPTER 4 EXPERIMENTAL STUDY OF THE OPTICAL PROPERTIES OF MIXED NANOFLUIDS

1) Overview

Experiments on nanofluids have been conducted mainly about increases in thermal conductivity and convection. A relatively small amount of experimental research efforts have been focused on the optical properties of nanofluids. However, there are some reported studies on the optical properties of dispersed systems. Baillis et al. gave a good review of experimental studies of dispersed media [84]. Osinga et al. [85] studied the extinction coefficient of packed-bed ($200 - 300\ \mu m$) particulate media. Otanicar et al. [36] and Kameya et al. [86] developed an explicit method to interpret the results from transmission measurements to determine the real and imaginary parts of the complex refractive index of the liquid cell in a layered system. Taylor et al. [37] characterized the optical properties of nanofluids using the same method.

In this chapter, I use the same method [36,82] to analyze the optical responses of mixed nanofluids. Very little work has been done on the thermophysical properties of mixed nanofluids, which means more than one kind of nanoparticle dispersed in a single base fluid. The motivation of this research is to look into the mixed nanofluids radiative properties. This study could be applied not only in a

solar collector for a DAC system, but also be valuable for applications where the nanofluids serve as a chemical reaction bed for photothermal or photocatalysis reactions.

In order to conduct experiments on nanofluids, first of all it is necessary to synthesize stable mixed nanofluids. The "off-the-shelf" dry solid nanoparticles are bought at the desired size and dispersed in base fluid (water) at a specified volume fraction. In order to avoid agglomeration, stabilizer and sonication are needed. Nanoparticles and 1% sodium dodecyl sulfate (a surfactant) are dispersed into the base fluid using a sonicator (a UP200 from Hielscher Ultrasonics GmbH, Teltow, Germany) for 15 to 30 min (amplitude 80%-100%) for all the fluids tested here. For comparison, all the volume fractions of the nanofluids are kept the same. Note for the mixed fluids that each kind of nanofluid has the same volume fraction, and the summation of the mixed nanofluids is the same as a fluid with only a single type of nanoparticle.

2) Numerical Method

A UV-VIS-NIR spectrophotometer is used to measure the optical properties which covers most of the solar spectrum (between 0.20 to 3 μm). This is a device that sends a light beam of adjustable wavelength through a sample cell and then measures the transmitted beam, see figure 12. I utilized a Jasco V-670 (Jasco

Corp., Great Dunmow, Essex, UK) spectrophotometer which could take measurements in the range of 0.19 to 2.7 μm.

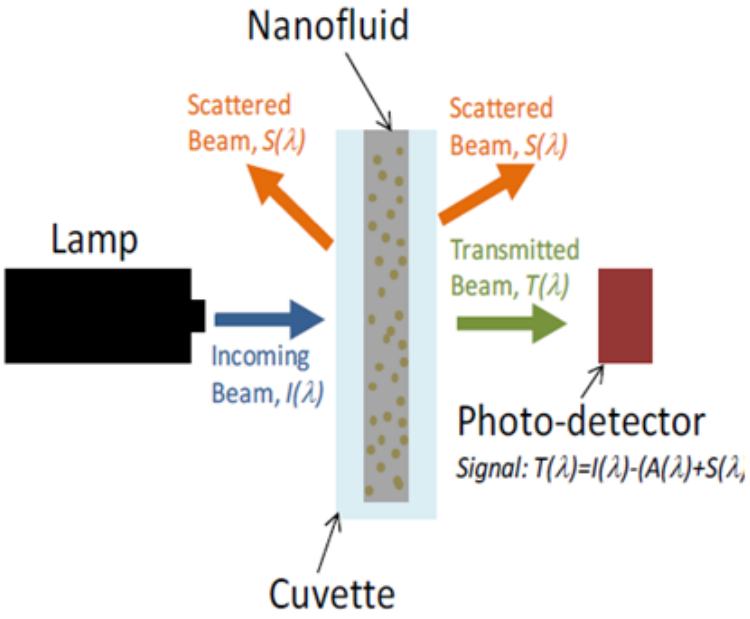

Figure 12 Experimental setup for measuring the optical and radiative properties of nanofluids [36]

After obtaining results from the spectrophotometer, further calculations are required to determine the extinction coefficients for nanofluids. Since a cuvette sample is a 'three-slab system' which contains two quartz windows and a liquid layer, multiple reflections at each interface need to be included in the analysis. Figure 13 shows the details of this multi-component system [37].

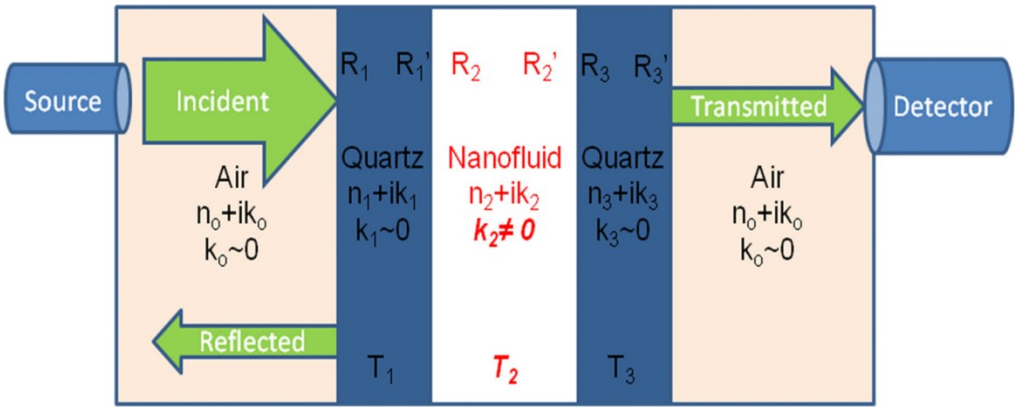

Figure 13 Three slab system[37]

To derive the optical constants of the sample (nanofluid), the first step is to calculate the values of reflection *R* and transmission *T* shown in Figure13 with the approach of Large et al. [87]:

$$R_i = \frac{(n_j - n_i)^2 + (k_j - k_i)^2}{(n_j + n_i)^2 + (k_j + k_i)^2} \tag{40}$$

$$T_i = \frac{(1 - R_i R_i')e^{-4\pi k_i L_i/\lambda}}{1 - R_i R_i' e^{-8\pi k_i L_i/\lambda}} \tag{41}$$

The variables n_i and k_i in the previous equations represent the *i*th spectral real and imaginary components of the refractive index. The quartz and air optical constants can be easily found in reference books [76]. *L* denotes the length of the *i*th element. Then the combined reflection and transmission are found[87]:

$$R = R_1 + \frac{T_1^2 R_2}{1 - R_2 R_1'} \tag{42}$$

$$R' = R_2' + \frac{T_2^2 R_1'}{1 - R_2 R_1'} \tag{43}$$

$$T = T_1 T_2 + \frac{R_1 R_2 T_1 T_2}{1 - R_2 R_1'} \tag{44}$$

Next the formula is applied to the three-slab system:

$$[R_T \; R_T' \; T_T] = [R_1 \; R_1' \; T_1] \oplus [R_2 \; R_2' \; T_2] \oplus [R_3 \; R_3' \; T_3] \tag{45}$$

With the above equations, use iterative calculation and the experimental result to get the imaginary part of the nanofluid index of refraction, and then use equation 22 to get the extinction coefficient $\sigma_{\exp}$.

3) Results and Discussion

With all the experimental techniques and calculation procedures, the mixing nanofluids' optical responses are revealed.

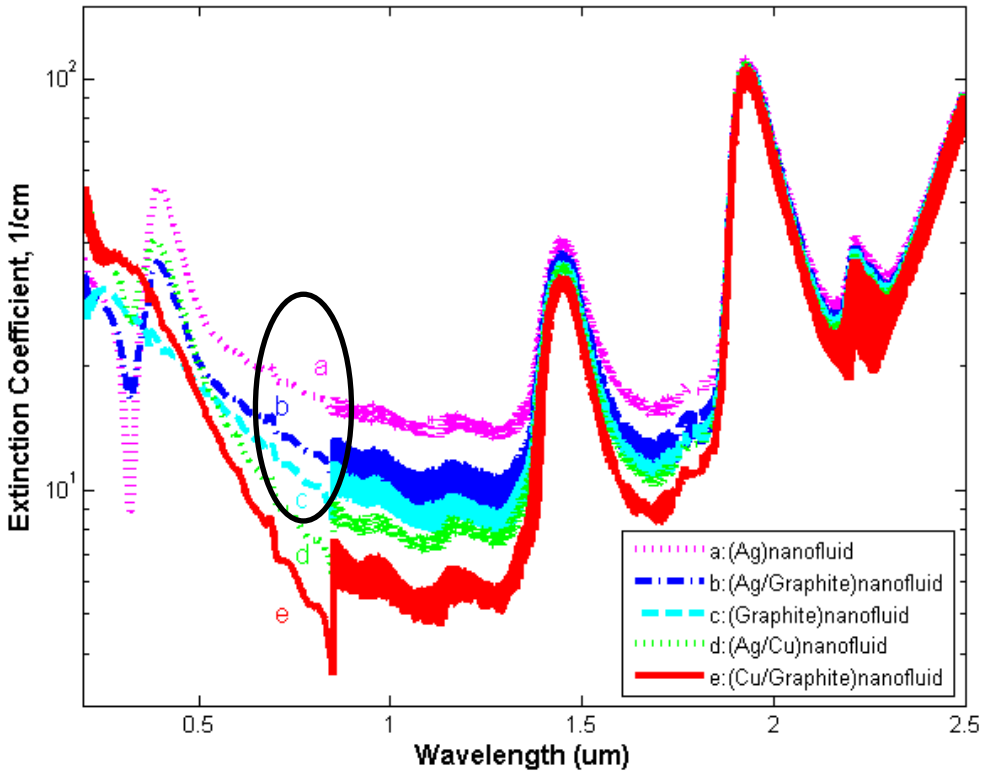

Figure 14 Extinction coefficients of single and mixed nanofluids

From figure 14, the mixed nanofluids' optical response is obtained. All the single and mixed nanofluids are at identical concentration (0.004% volume fraction). The extinction spectrum of Cu nanofluid is omitted since there is strong noise in the result. Considering the 0.004% volume fraction of Silver and Graphite nanofluids and their mixed result (curves a, b, c in figure 14), the mixed

nanofluid exhibits the combined extinction coefficients which are "generally" linearly added. However, since the extinction coefficient is wavelength dependent, at some wavelengths the mixed result is not simply the addition of the two single-inclusion nanofluids. Apparently, further research is necessary to precisely predict the mixed nanofluids' optical response.

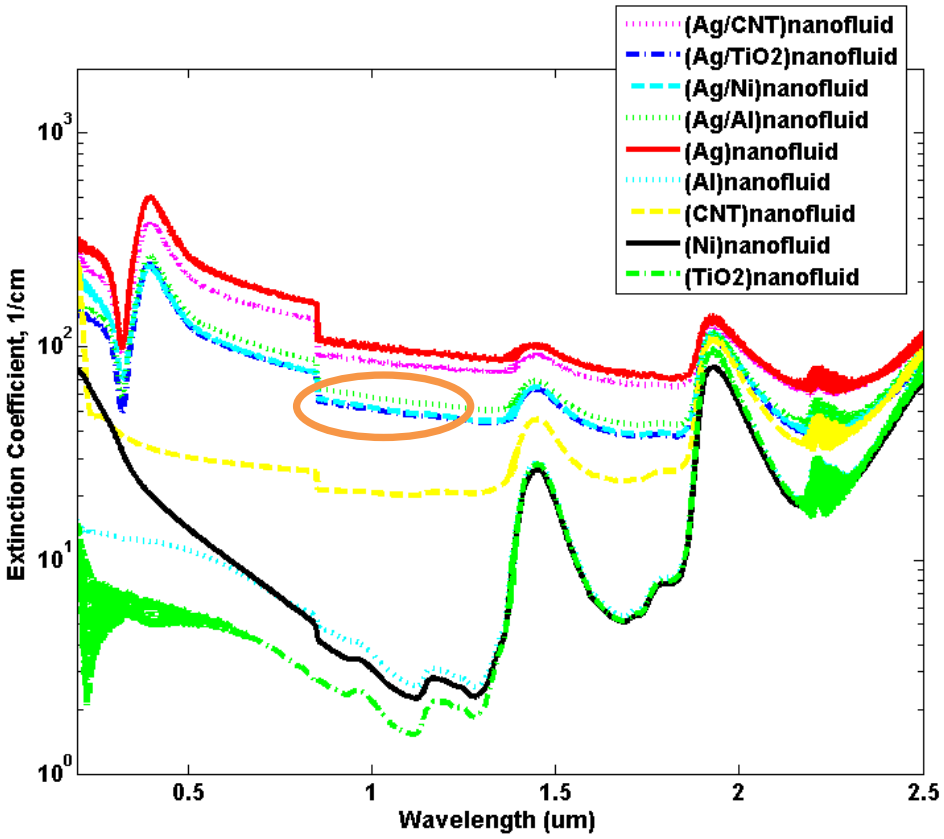

Figure 15 Extinction coefficients of single and mixed nanofluids at high concentration (0.04% volume fraction)

Figure 15 shows the mixed nanofluids' extinction coefficients at high concentration (0.04% concentration). For the single-inclusion sulotion, the

volume fraction is identical except for the CNT nanofluid whose concentration is unknown. As for the mixed nanofluids, the same volume of two different nanolfuids was simply added together to maintain the concentration of the inclusions at 0.04% as well. An interesting pheomenon is that when Al, Ni and TiO_2 nanofluids are mixed with Ag nanofluid at the same volume fraction, their mixed nanofluids' extinction spectra are almost identical (as marked in figure 15). On the other hand, it is easy to distingush the difference between pure Al, Ni and TiO_2 nanofluid's extinction coefficients. Hence, a conclusion can be made that at some concentrations, the inclusion that exhibits strong extinction coefficient over some spectrum will be dominant when it is mixed with other nanofluids that have a weak extinction coefficent over that same spectrum. The author thinks it may be caused by the strong coupling effect beween Ag nanoparticles. In other words, the strong surface plasmon response effect between plasmonic particles dominates this behavior. However, much more work needs to be done to quantitatively explain this phenomenon.

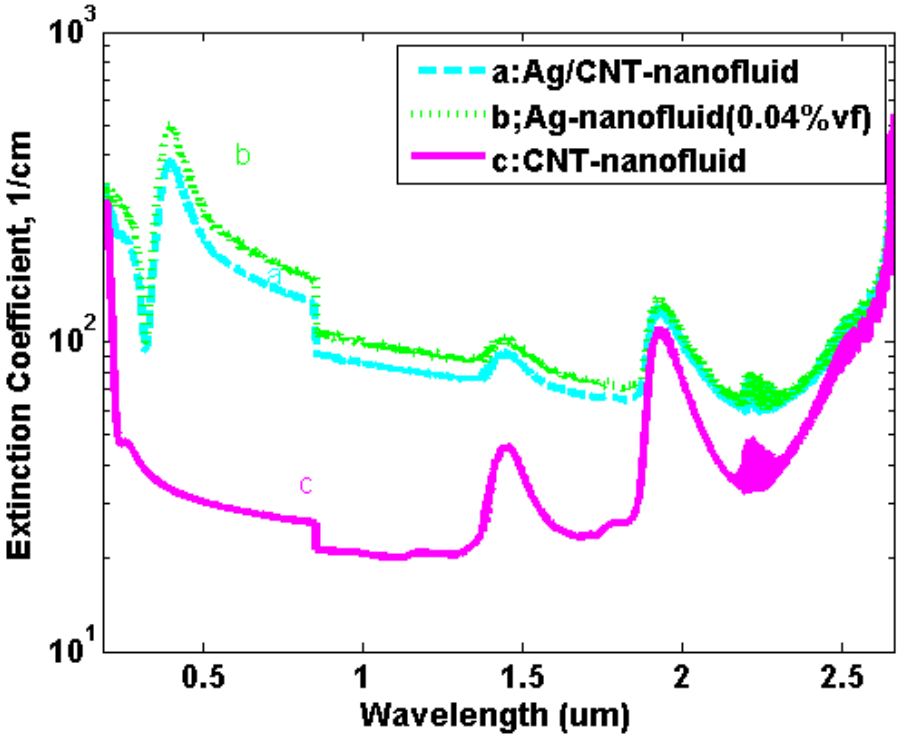
a:Ag/CNT-nanofluid
b;Ag-nanofluid(0.04%vf)
c:CNT-nanofluid
b
c
Extinction Coefficient, 1/cm
Wavelength (um)
10^3
10^2
10^1
0.5
1
1.5
2
2.5

(a)

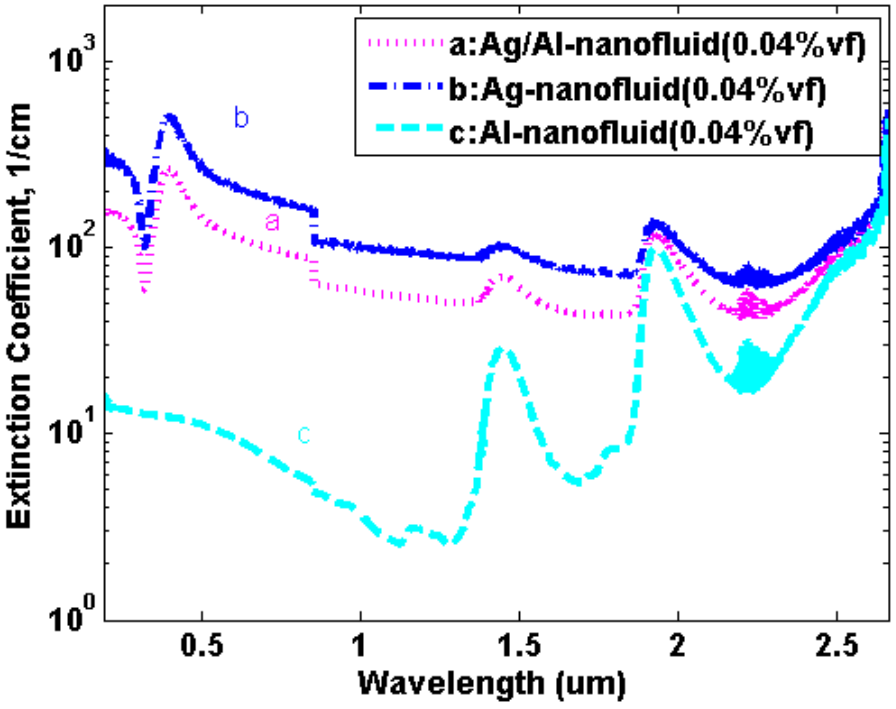
a:Ag/Al-nanofluid(0.04%vf)
b:Ag-nanofluid(0.04%vf)
c:Al-nanofluid(0.04%vf)
Extinction Coefficient, 1/cm
Wavelength (um)
a
b
c

(b)

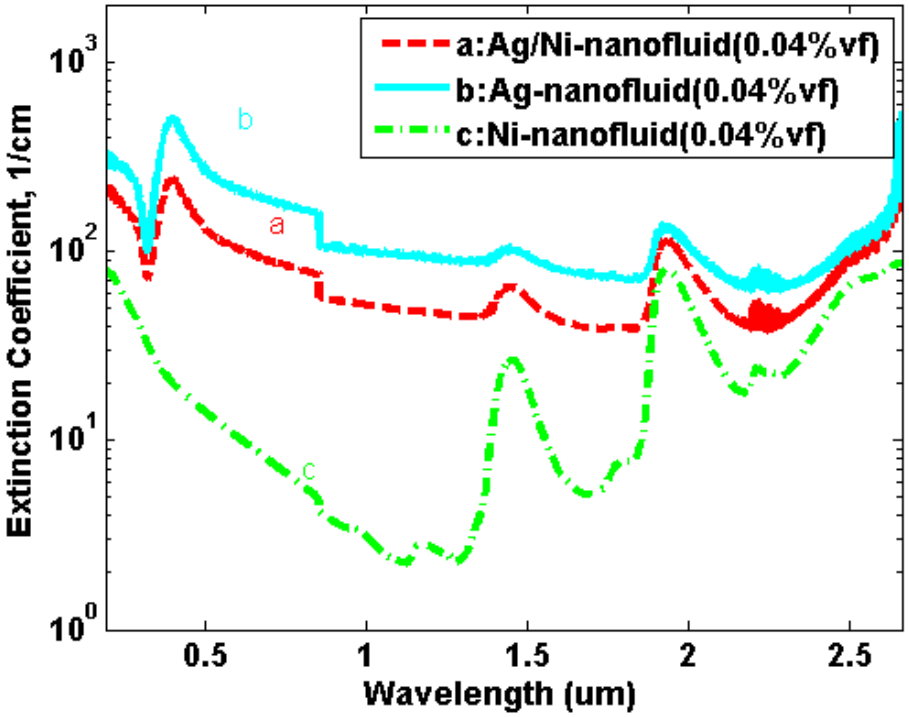
a:Ag/Ni-nanofluid(0.04%vf)
b:Ag-nanofluid(0.04%vf)
c:Ni-nanofluid(0.04%vf)
Extinction Coefficient, 1/cm
Wavelength (um)
a
b
c

(c)

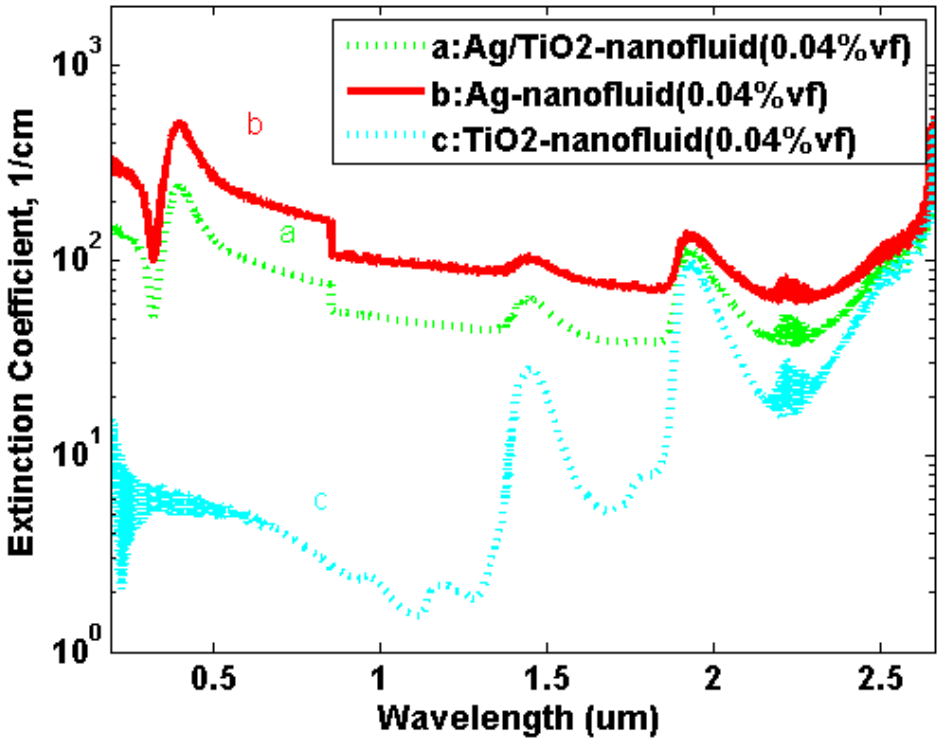

(d)

Figure 16 Single and mixed nanofluids' extinction spectra comparison: (a) Ag-Al-nanofluids（0.04%volume fraction); (b) Ag-CNT-nanofluids （0.04%volume fraction Ag nanofluids + unknown concentration CNT nanofluids）; (c) Ag-Ni-nanofluids（0.04%volume fraction）; (d) Ag-TiO_2-nanofluids（0.04%volume fraction）.

In Ag and CNT nanofluids, the Ag concentration is maintained at 0.04% and with the same volume of CNT nanofluid. From figure 16, the extinction spectrum of Ag/CNT nanofluids seems to be almost identical to that of Ag nanofluids at the

same volume fraction. Hardly any effect can be observed to be caused by the CNT nanofluid. Figure 16 (b,c and d) are Ag nanofluids (0.04%) mixed with three different nanofluids (0.04%volume fraction) respectively. The Al, Ni and TiO_2 nanofluids exhibit different extinction spectra. However, when they are mixed with Ag nanofluids, the mixed nanofluids demonstrate quite similar optical responses. A conculsion can be made from figure 16 that the mixed nanofluids' extinction spectra are not a simple addition of each single inclusion nanofluid's extinction coefficients. Again, the inclusion that has a strong extinction coefficient over some spectral range will be dominant for the mixed nanofluids' optical response over that spectral range.

CHAPTER 5 CORE-SHELL PHOTOCATALYST

1) Overview

From the previous chapters, core-shell nanoparticles demonstrate strong surface plasmon effect and tunable plasmon frequency due to the Coulombic force manifested at two dissimilar dielectric interfaces [88]. By tuning the surface plasmon frequency, the single nanostructure's optical response and corresponding optical properties can be controlled.

In 1972, Fujishimna and Honda discovered the photocatalytic splitting of water on TiO_2 electrodes [89]. This event is considered to be the beginning of a new age in heterogeneous photocatalysis. Photocatalysis is a reaction which utilizes electromagnetic radiation to activate a substance which modifies the rate of a chemical reaction without being involved itself. Semiconductors are often selected as photocatalysts due to a narrow gap between the valence and conduction bands. The semiconductors need to absorb energy equal to or more than its energy gap to enable photocatalysis [90]. This movement of electrons forms electron-hole pairs. The hole can oxidize donor molecules. Titanium Dioxide is most widely used among other semiconductors since it has many advantages. It is inert，resistant to corrosion, highly photoactive，and needs little post-processing, making it inexpensive [90]. What's more, it can react under mild

operating conditions. It has also been widely employed in most environmental applications, such as water purification, treatment of water polluted with toxic substances, hazardous waste control [91]， and conversion of CO_2 into more useful compounds [92].

Nevertheless, it requires ultraviolet light for photocatalysis to occur， which implies using only 4% of the solar energy absorption, resulting in low efficiency [93] . The major challenge of using TiO_2 for photocatalysis is to efficiently absorb the sunlight. A lot of researchers have been working on this problem. The Kamat group has performed considerable work on titania nanoparticles photocatalysis, semiconductor-metal [94,95], and semiconductor-reduced graphene oxide (RGO) nano-assemblies [96] to increase the efficiency of the photocatalysis. Our approach to increase the efficiency of solar-induced titania photocatalysis is not only to focus on tuning the band-gap of titania nanoparticles, but also to exploit plasmonic nanostructures, more specifically core-shell structures, to concentrate more light energy at the spectrum corresponding to the bandgap. There are several advantages and possibilities for this new structure which is different from Kamat et al's previous work on noble metal shell titania core structures [95,97]. First of all, by using a thin titania shell, one can increase the contact surface compared to the same amount of solid titania nanoparticles. Secondly,

the metallic core material and size can be optimized to produce a surface plasmon frequency that intersects with the TiO_2 (Rutile)band gap frequency (387nm), in order to maximize the solar absorption efficiency. Thirdly, the thin layer of TiO_2 shell may exhibit a quantum size effect which will tune its own bandgap. Fourthly, the metallic core can generate localized heat by the surface plasmon resonance effect, which would allow "hot" electrons to cross the band gaps easily.

2) Results and Discussion

I have conducted a preliminary calculation of the surface plasmon effect on metal-core TiO_2 shell nanoparticles to show some potential of this idea. The same approach is applied here as was done for the metallic shell dielectric core nanoparticles described previously. The quasi-static approximation is assumed and the particles are in the Rayleigh regime. Note: in this analysis, electron or charge transport between metal and semiconductor, and corresponding work function changes are not considered. Also the size effect on the TiO_2 bandgap is out of our scope here. In figure 16 (a), the absorption efficiency of single solid TiO_2 nanoparticles at different radius (r) are plotted. The bandgap and solar spectrum are also shown for comparison. As for the core-shell nanoparticles (b, c, d, e in figure16), the radius (r_2) of the total particle is held constant at

25 nm, and the shell thickness (r_2-r_1) changes from 2 nm to 10nm respectively. The sizes of the core-shell nanoparticles are kept the same in order to eliminate any size effects on the magnitude of the absorption efficiency.

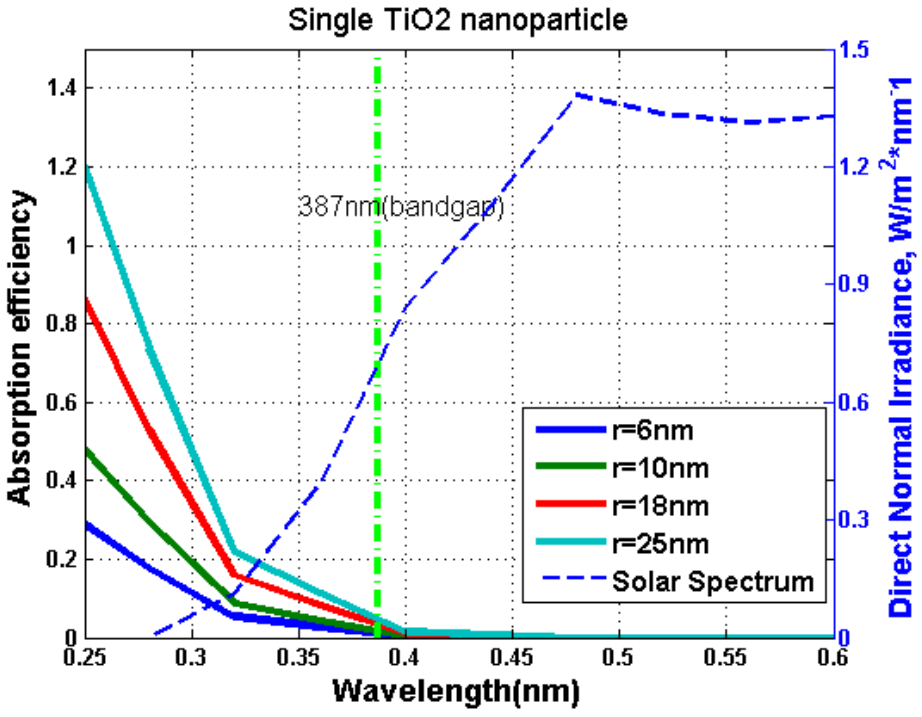

（a）

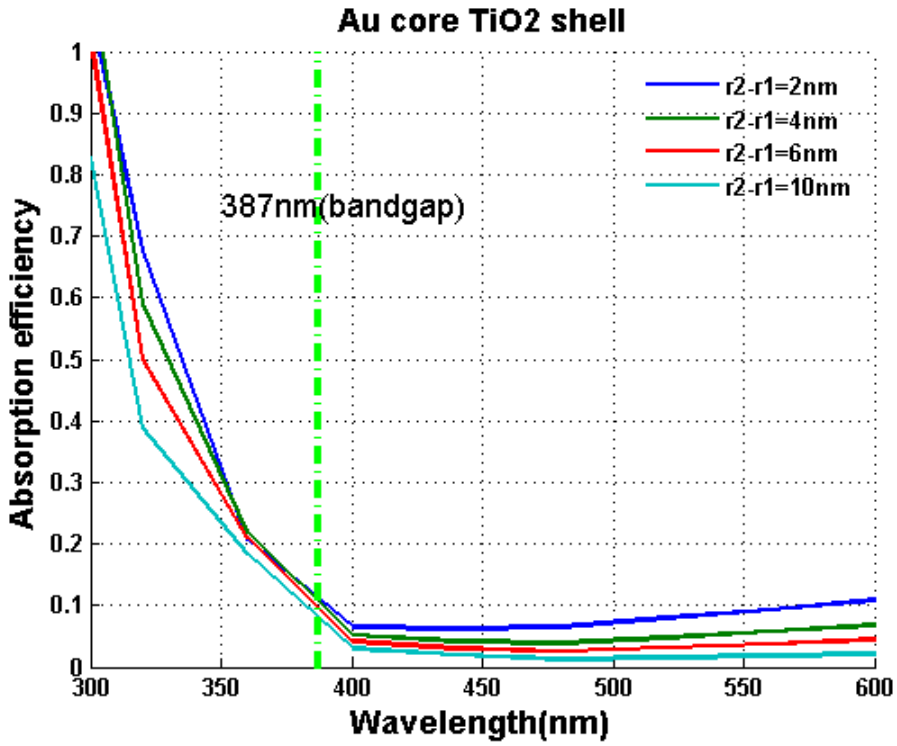
Au core TiO2 shell
r2-r1=2nm
r2-r1=4nm
r2-r1=6nm
r2-r1=10nm
387nm(bandgap)
Absorption efficiency
Wavelength(nm)
0
0.1
0.2
0.3
0.4
0.5
0.6
0.7
0.8
0.9
1
300
350
400
450
500
550
600

(b)

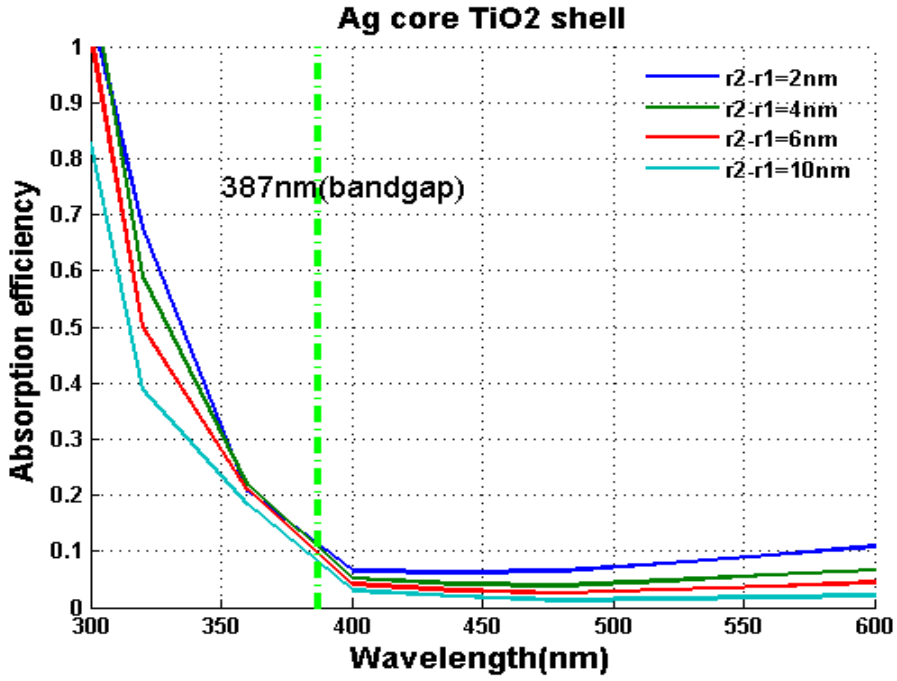
Ag core TiO2 shell
r2-r1=2nm
r2-r1=4nm
r2-r1=6nm
r2-r1=10nm
387nm(bandgap)
Absorption efficiency
Wavelength(nm)
0
0.1
0.2
0.3
0.4
0.5
0.6
0.7
0.8
0.9
1
300
350
400
450
500
550
600

(c)

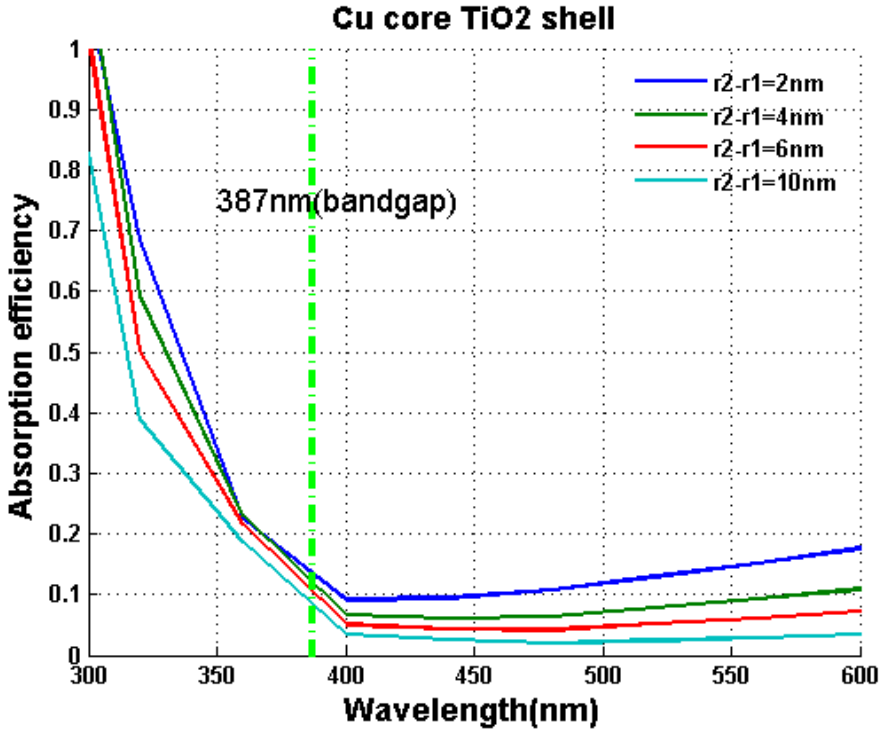
Cu core TiO2 shell
r2-r1=2nm
r2-r1=4nm
r2-r1=6nm
r2-r1=10nm
387nm(bandgap)
Absorption efficiency
Wavelength(nm)
0
0.1
0.2
0.3
0.4
0.5
0.6
0.7
0.8
0.9
1
300
350
400
450
500
550
600

(d)

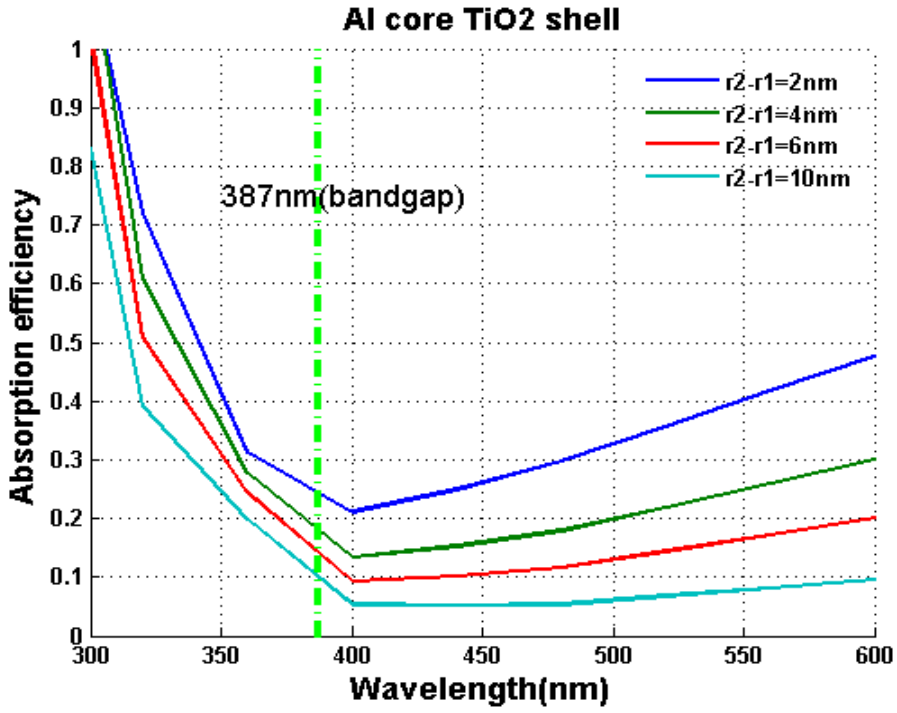
Al core TiO2 shell
r2-r1=2nm
r2-r1=4nm
r2-r1=6nm
r2-r1=10nm
387nm(bandgap)
Absorption efficiency
Wavelength(nm)
0
0.1
0.2
0.3
0.4
0.5
0.6
0.7
0.8
0.9
1
300
350
400
450
500
550
600

(e)

Figure 17 Absorption efficiency of single core-shell nanoparticles from 300 nm to 800 nm, (a) solid TiO_2 nanoparticles (b) Au/ TiO_2 core-shell nanoparticles (c) Ag/ TiO_2 core-shell nanoparticles (d) Cu/ TiO_2 core-shell nanoparticles (e) Al/ TiO_2 core-shell nanoparticles

From figure 17, the Al/TiO_2 core-shell nanostructure has the best absorption efficiency in the UV region where the TiO_2 band is < 387nm. The thinner the TiO_2 shell is, the higher the absorption efficiency.

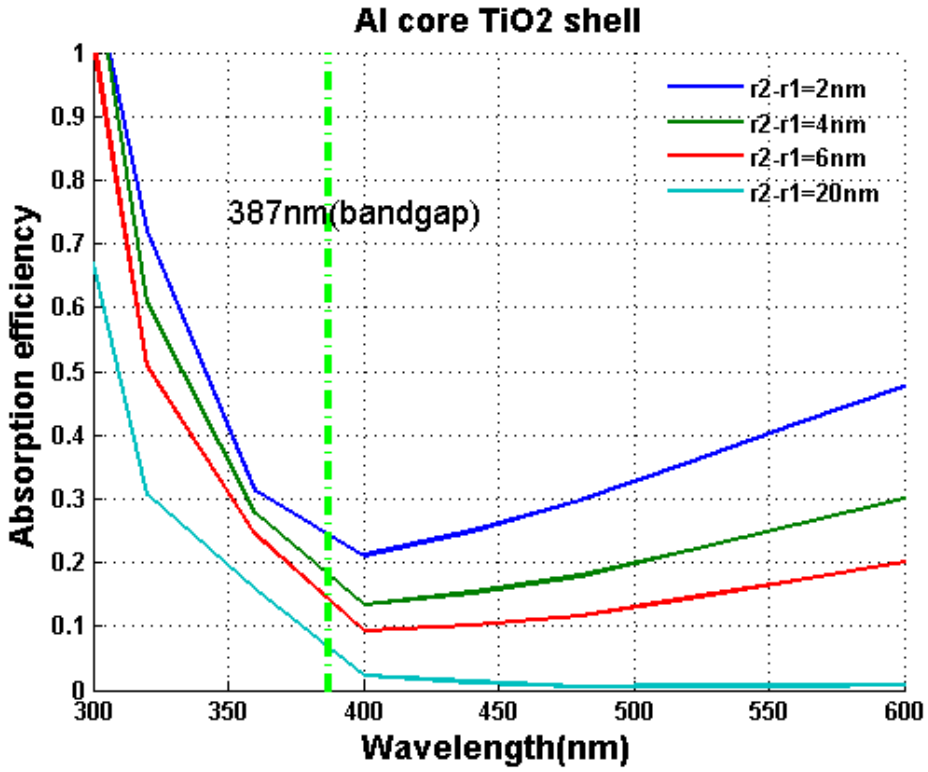

Figure 18 Absorption efficiency of a single Al/ TiO_2 core-shell nanoparticle from 300 nm to 600 nm

Figure 18 demonstrates the effect of the TiO_2 shell thickness on the core-shell nanoparticle's absorption efficiency. The thinner TiO_2 shell is, the better the absorption efficiency is. Considering a shell thickness of 20 nm (more like a solid TiO_2 nanoparticle) compared to a shell thickness of 2 nm, there is a large difference in the absorption coefficient, which is promising to concentrate more solar energy near the bandgap of titania.

Because of the wave-particle duality, electrons have thermal de Broglie wavelength. A rough prediction can be made by the following equation [98]:

$$\lambda_e = \frac{\hbar}{\sqrt{2\pi mkT}} \tag{46}$$

where $\hbar$ is Planck's constant divided by 2π, m the effective electron mass, and k the Boltzmann constant. For TiO_2, the electron effective mass $m=10*m_0$ [99]. From equation 46, the de Broglie wavelength of electrons in TiO_2 is about 1.9967×10^{-10} (m), or 0.2 nm. This suggests that even at the thinnest TiO_2 shell thicknesses considered here (2 nm), there will likely be an insignificant size effect on the bandgap.

CHAPTER 6 CONCLUSION AND FUTURE WORK

1) General Conclusions

This research involves two cutting-edge technologies: nanofluids and plasmonics. Specifically, a numerical model for predicting the core-shell nanoparticles' optical response in the Rayleigh regime is provided. These results are then applied in a volumetric absorption model. A detailed analysis applying core-shell nanoparticle suspensions in a direct solar collector system is given. A simple calculation on core-shell TiO_2 nanoparticles' optical response has also been studied here. Experiments on mixed nanofluids' extinction coefficients have been conducted.

Much of the work is modified from previous researchers' work, especially on volumetric absorption [14,49,54] and optical measurements [36,37]. A model for predicting the optical properties of core-shell nanoparticle suspensions, however, is introduced here, as are experimental measurements of the extinction coefficients of mixed nanofluids.

Most of the contents in the previous chapters have been reported to the scientific community through various publications:

1. A review of current and historical researches on nanofluids, plasmonics and radiation heat transfer. (Published in ASME 2012 MNHMT conference and submitted to the *Journal of Applied Physics*)
2. The plasmonic nanoparticle suspensions' optical response modeling, in other words, metal-shell dielectric-core nanoparticle suspensions' radiative properties. (presented and published in the ASME 2012 MNHMT conference and submitted to the Journal of Solar Energy Engineering)
3. Comparison of different nanoparticle suspensions' spectral radiative properties and corresponding application to direct solar collector. (Presented and published in the ASME 2012 Summer HT conference, and awaiting compilation into a journal paper)

2) Future Work

More work is needed for further studying plasmonics in energy harvesting applications. Especially on the photocatalysis research, a great amount of work will be necessary on both modeling and experiments.

1) Core-shell structure modeling: To go to large size particles (r > 50nm), Mie scattering theory is needed. FDTD and DDA are better numerical methods

than the Rayleigh assumption for conditions of arbitrary shape and discontinuity of the shell;

2) Disperse medium modeling: Incorporate the in-scattering term by using differential-discrete-ordinate or Montel Carlo method;
3) Synthesize stable core-shell nanostructures which can be tested and applied under high-temperature conditions;
4) More modeling and experimental work on the temperature effect of core-shell nanoparticles is necessary to characterize the core-shell nanoparticle suspensions' thermophysical properties;
5) Photocatalysis: The DDA method [100] and the FDTD method [101] have been used for predicting the near-field enhancement of the plasmonic nanoparticles' influence on photocatalysis reaction;
6) Look for other possible applications of using core-shell nanostructures.

REFERENCES

[1] Choi S. U. S., and Eastman J. A., 1995, "Enhancing thermal conductivity of fluids with nanoparticles," ASME 1995 Int. Mech. Eng. Congress & Exposition., Argonne, IL.

[2] Vollath D., 2007, "Plasma synthesis of nanoparticles," Kona, **1**(25), pp. 39-55.

[3] Ghadimi A., Saidur R., and Metselaar H. S. C., 2011, "A review of nanofluid stability properties and characterization in stationary conditions," International Journal of Heat and Mass Transfer, **54**(17-18), pp. 4051-4068.

[4] Fang X., Xuan Y., and Li Q., 2009, "Experimental investigation on enhanced mass transfer in nanofluids," Applied Physics Letters, **95**(20), p. 203108.

[5] Veilleux J., and Coulombe S., 2011, "A dispersion model of enhanced mass diffusion in nanofluids," Chemical Engineering Science, **66**(11), pp. 2377-2384.

[6] Kedzierski M. a., 2009, "Effect of CuO nanoparticle concentration on R134a/lubricant pool-boiling heat transfer," J. of Heat Transfer, **131**(4), p. 043205.

[7] Peng H., Ding G., Jiang W., Hu H., and Gao Y., 2009, "Heat transfer characteristics of refrigerant-based nanofluid flow boiling inside a horizontal smooth tube," International Journal of Refrigeration, **32**(6), pp. 1259-1270.

[8] Murshed S. M. S., Nieto de Castro C. a., Lourenço M. J. V., Lopes M. L. M., and Santos F. J. V., 2011, "A review of boiling and convective heat transfer with nanofluids," Renewable and Sustainable Energy Reviews, **15**(5), pp. 2342-2354.

[9] Wen D., Lin G., Vafaei S., and Zhang K., 2009, "Review of nanofluids for heat transfer applications," Particuology, **7**(2), pp. 141-150.

[10] Piatkowski N., Wieckert C., and Steinfeld A., 2009, "Experimental investigation of a packed-bed solar reactor for the steam-gasification of carbonaceous feedstocks," Fuel Processing Technology, **90**(3), pp. 360-366.

[11] Kim S. H., Choi S. R., and Kim D., 2007, "Thermal conductivity of metal-oxide nanofluids: Particle size dependence and effect of laser irradiation," J. of Heat Transfer, **129**(3), p. 298.

[12] Taylor R. A., Phelan P. E., Adrian R. J., and Prasher R. S., 2009, "Experimental results for light-induced boiling in water-based graphite nanoparticle suspensions," Proc. of the ASME 2009 Summer Heat Transfer Conf., ASME, pp. 1-9.

[13] Peer D., Karp J. M., Hong S., Farokhzad O. C., Margalit R., and Langer R., 2007, "Nanocarriers as an emerging platform for cancer therapy.," Nature nanotechnology, **2**(12), pp. 751-60.

[14] Taylor R. A., Phelan P. E., Otanicar T. P., Walker C. a., Nguyen M., Trimble S., and Prasher R. S., 2011, "Applicability of nanofluids in high flux solar collectors," Journal of Renewable and Sustainable Energy, **3**(2), p. 023104.

[15] Zou S., and Schatz G. C., 2004, "Narrow plasmonic/photonic extinction and scattering line shapes for one and two dimensional silver nanoparticle arrays.," The Journal of chemical physics, **121**(24), pp. 12606-12.

[16] Khlebtsov N. G., Trachuk L. a., and Mel'nikov a. G., 2005, "The effect of the size, shape, and structure of metal nanoparticles on the dependence of their optical properties on the refractive index of a disperse medium," Optics and Spectroscopy, **98**(1), pp. 77-83.

[17] Dice G. D., Mujumdar S., and Elezzabi a. Y., 2005, "Plasmonically enhanced diffusive and subdiffusive metal nanoparticle-dye random laser," Applied Physics Letters, **86**(13), p. 131105.

[18] Schwartzberg A. M., and Zhang J. Z., 2008, "Novel Optical Properties and Emerging Applications of Metal Nanostructures," Journal of Physical Chemistry C, **112**(28), pp. 10323-10337.

[19] Garcia G., Buonsanti R., Runnerstrom E. L., Mendelsberg R. J., Llordes A., Anders A., Richardson T. J., and Milliron D. J., 2011, "Dynamically Modulating the Surface Plasmon Resonance of Doped Semiconductor Nanocrystals.," Nano letters.

[20] Reena Mary a P., Suchand Sandeep C. S., Narayanan T. N., Philip R., Moloney P., Ajayan P. M., and Anantharaman M. R., 2011, "Nonlinear and magneto-optical transmission studies on magnetic nanofluids of non-interacting metallic nickel nanoparticles.," Nanotechnology, **22**(37), p. 375702.

[21] Lee J.-C., Seo H.-S., and Kim Y.-J., 2011, "Experimental study on the dielectric breakdown performance with magnetic field and concentrations of magnetic nanofluids," International Communications in Heat and Mass Transfer, **1**.

[22] Konakanchi H., Vajjha R., Misra D., and Das D., 2011, "Electrical conductivity measurements of nanofluids and development of new correlations," Journal of Nanoscience and Nanotechnology, **11**(8), pp. 6788-6795.

[23] Tyagi H., 2008, "Radiative and combustion properties of nanoparticle-laden liquids," Arizona State University.

[24] Prasher R. S., and Phelan P. E., 2005, "Modeling of Radiative and Optical Behavior of Nanofluids Based on Multiple and Dependent Scattering Theories," Heat Transfer, Part B, **2005**, pp. 739-743.

[25] Gentle a R., and Smith G. B., 2010, "Radiative heat pumping from the Earth using surface phonon resonant nanoparticles.," Nano letters, **10**(2), pp. 373-9.

[26] Mie G., 1908, "Beiträge zur Optik trüber Medien, speziell kolloidaler Metallösungen," Ann. Physik.

[27] Bohren C. F. ., and Huffman D. R., 1998, Absorption and Scattering of Light by Small Particles (Wiley science paperback series), Wiley-VCH, Weinheim, Germany.

[28] Hulst H. C. van de, 1981, Light Scattering by Small Particles (Structure of Matter Series), Dover Publications.

[29] Modest M. F., 2003, Radiative Heat Transfer, 2nd Edition, Academic Press.

[30] U. Kreibig;, and V. Vollmer, 1995, Optical Properties of Metal Clusters (Springer Series in Materials Science), Springer, Berlin.

[31] Abdelrahman M., Fumeaux P., and Suter P., 1979, "Study of solid-gas-suspensions used for direct absorption of concentrated solar radiation," Solar Energy, **22**(1), pp. 45-48.

[32] Hunt A. J., 1978, Small Particle Heat Exchangers.

[33] Karni J., Kribus a., Rubin R., and Doron P., 1998, "The 'Porcupine': A Novel High-Flux Absorber for Volumetric Solar Receivers," Journal of Solar Energy Engineering, **120**(2), p. 85.

[34] Kumar S., and Tien C. L., 1990, "Dependent absorption and extinction of radiation by small particles," Journal of Heat Transfer (Transactions of the ASME (American Society of Mechanical Engineers), Series C); (United States), **112:1**.

[35] Tien C. L., 1988, "Thermal Radiation in Packed and Fluidized Beds," J. of Heat Transfer, **110**(4b), p. 1230.

[36] Otanicar T. P., Phelan P. E., and Golden J. S., 2009, "Optical properties of liquids for direct absorption solar thermal energy systems," Solar Energy, **83**(7), pp. 969-977.

[37] Taylor R. A., Phelan P. E., Otanicar T. P., Adrian R. J., and Prasher R. S., 2011, "Nanofluid optical property characterization: towards efficient direct absorption solar collectors.," Nanoscale research letters, **6**(1), p. 225.

[38] Taylor R. A., Phelan P. E., Adrian R. J., Gunawan A., and Otanicar T. P., 2012, "Characterization of light-induced, volumetric steam generation in nanofluids," International Journal of Thermal Sciences, **56**, pp. 1-11.

[39] Andresen P., Bath A., Groger W., Meijer G., and Meulen J. J., 1988, "Laser-induced fluorescence with tunable excimer lasers as a possible method for instantaneous temperature field measurements at high pressures : checks with an atmospheric flame," Applied Optics, **27**(2), pp. 365-378.

[40] Steinfeld A., and Schubnell M., 1993, "Optimum aperature size and operating temperature of a solar cavity-receiver," Solar Energy, **50**(1), pp. 19-25.

[41] Miller F. J., and Koenigsdorff R. W., 2000, "Thermal modeling of a small-particle solar central," Journal of Solar Energy Engineering, **122**(1), pp. 23-29.

[42] Bertocchi R., Kribus A., and Karni J., 2004, "Experimentally determined optical properties of a polydisperse carbon black cloud for a solar particle receiver," Journal of Solar Energy Engineering, **126**(3), p. 833.

[43] Haussener S., Hirsch D., Perkins C., Weimer A., Lewandowski A., and Steinfeld A., 2009, "Modeling of a multitube high-temperature solar thermochemical reactor for hydrogen production," Journal of Solar Energy Engineering, **131**(2), p. 024503.

[44] Kumar S., Majumdar a., and Tien C. L., 1990, "The Differential-Discrete-Ordinate Method for Solutions of the Equation of Radiative Transfer," J. of Heat Transfer, **112**(2), p. 424.

[45] Merabia S., Keblinski P., Joly L., Lewis L. J., and Barrat J.-louis, 2009, "Critical heat flux around strongly heated nanoparticles," Heat and Mass Transfer, pp. 1-4.

[46] Lenert A., Zuniga Y. S. P., and Wang E. N., 2010, "Nanofluid-based absorpers for high temperature direct solar collectors," IHTC14-22208, pp. 1-10.

[47] Natarajan E., and Sathish R., 2009, "Role of nanofluids in solar water heater," The International Journal of Advanced Manufacturing Technology, pp. 3-7.

[48] Taylor R. A., Phelan P. E., Otanicar T. P., and Trimble S., 2010, "Applicability of nanofluids in concentrated solar energy harvesting," ES2010-90055, pp. 1-8.

[49] Otanicar T. P., Phelan P. E., Prasher R. S., Rosengarten G., and Taylor R. A., 2010, "Nanofluid-based direct absorption solar collector," Journal of Renewable and Sustainable Energy, **2**(3), p. 033102.

[50] Sani E., Mercatelli L., Barison S., Pagura C., Agresti F., Colla L., and Sansoni P., 2011, "Potential of carbon nanohorn-based suspensions for solar thermal collectors," Solar Energy Materials and Solar Cells, **95**(11), pp. 2994-3000.

[51] Otanicar T. P., Phelan P. E., Taylor R. A., and Tyagi H., 2011, "Spatially Varying Extinction Coefficient for Direct Absorption Solar Thermal Collector Optimization," Journal of Solar Energy Engineering, **133**(May), pp. 1-7.

[52] Taylor R. A., Phelan P. E., Otanicar T. P., Adrian R. J., and Prasher R. S., 2009, "Vapor Generation in a Nanoparticle Liquid Suspension Using a Focused , Continuous Laser Beam," Applied Physics Letters.

[53] Kumar S., and Tien C. L., 1990, "Analysis of Combined Radiation and Convection in a Particulate-Laden Liquid Film," Journal of Solar Energy Engineering, **112**(4), p. 293.

[54] Tyagi H., Phelan P., and Prasher R. S., 2009, "Predicted Efficiency of a Low-Temperature Nanofluid-Based Direct Absorption Solar Collector," Journal of Solar Energy Engineering, **131**(4), p. 041004.

[55] Otanicar T. P., 2009, "Direct absorption solar thermal collectors utlizing liquid-nanoparticle suspensions."

[56] Payne E. K., Shuford K. L., Park S., Schatz G. C., and Mirkin C. a, 2006, "Multipole plasmon resonances in gold nanorods.," The journal of physical chemistry. B, **110**(5), pp. 2150-4.

[57] Carotenuto G., Martorana B., Perlo P., and Nicolais L., 2003, "A universal method for the synthesis of metal and metal sulfide clusters embedded in polymer matrices," Journal of Materials Chemistry, **13**(12), p. 2927.

[58] Tessier P. M., Velev O. D., Kalambur A. T., Rabolt J. F., Lenhoff A. M., and Kaler E. W., 2000, "Assembly of gold nanostructured films templated by colloidal crystals and use in surface-enhanced raman spectroscopy," Journal of the American Chemical Society, **122**(39), pp. 9554-9555.

[59] Liu Z., Hou W., Pavaskar P., Aykol M., and Cronin S. B., 2011, "Plasmon resonant enhancement of photocatalytic water splitting under visible illumination.," Nano letters, **11**(3), pp. 1111-6.

[60] Torkamani S., Wani S. N., Tang Y. J., and Sureshkumar R., 2010, "Plasmon-enhanced microalgal growth in miniphotobioreactors," Applied Physics Letters, **97**(4), p. 043703.

[61] Neeves A. E., and Birnboim M. H., 1989, "Composite structures for the enhancement of nonlinear-optical susceptibility," Journal of the Optical Society of America B, **6**(4), p. 787.

[62] Averitt R. D., Westcott S. L., and Halas N. J., 1999, "Linear optical properties of gold nanoshells," Journal of the Optical Society of America B, **16**(10), p. 1824.

[63] Westcott S., Jackson J., Radloff C., and Halas N. J., 2002, "Relative contributions to the plasmon line shape of metal nanoshells," Physical Review B, **66**(15), pp. 1-5.

[64] Lal S., Link S., and Halas N. J., 2007, "Nano-optics from sensing to waveguiding," Nature Photonics, **1**(11), pp. 641-648.

[65] Grady N. K., Halas N. J., and Nordlander P., 2004, "Influence of dielectric function properties on the optical response of plasmon resonant metallic nanoparticles," Chemical Physics Letters, **399**(1-3), pp. 167-171.

[66] Kelly L. K., Coronado E., Zhao L. L., and Schatz G. C., 2003, "The optical properties of metal nanoparticles: The influence of size, shape, and dielectric environment," J.Phys.Chem.B, **107**(3), pp. 668-677.

[67] Zou S., Schatz G. C., Schatz G. C., and Introduction I., 2004, "Narrow plasmonic/photonic extinction and scattering line shapes for one and two dimensional silver nanoparticle arrays," J. of Chemical Physics, **121**(24), pp. 12606-12612.

[68] Lee B. J., Park K., Walsh T., and Xu L., 2012, "Radiative Heat Transfer Analysis in Plasmonic Nanofluids for Direct Solar Thermal Absorption," Journal of Solar Energy Engineering, **134**(2), p. 021009.

[69] Cole J. R., and Halas N. J., 2006, "Optimized plasmonic nanoparticle distributions for solar spectrum harvesting," Applied Physics Letters, **89**(15), p. 153120.

[70] Halas N., 2002, “The Optical Properties of Nanoshells,” Optics and Photonics News, **13**(8), p. 26.

[71] Jain P. K., Huang X., El-Sayed I. H., and El-Sayed M. a., 2007, “Review of Some Interesting Surface Plasmon Resonance-enhanced Properties of Noble Metal Nanoparticles and Their Applications to Biosystems,” Plasmonics, **2**(3), pp. 107-118.

[72] Kelly, K.L., Coronado, E., Zhao, l. l., and Schatz G. ., 2003, “The Optical Properties of Metal Nanoparticles: The Influence of Size, Shape, and Dielectric Environment,” J.Phys.Chem.B, **11**(3), pp. 668-677.

[73] L.Aden A., and Kerker M., 1951, “Scattering of Electromagnetic Waves from Two Concentric Spheres,” Journal of Applied Physics, **22**(1), pp. 1242-1246.

[74] Hao E., Li S., Bailey R. C., Zou S., Schatz G. C., and Hupp J. T., 2004, “Optical Properties of Metal Nanoshells,” The Journal of Physical Chemistry B, **108**(4), pp. 1224-1229.

[75] Prasher R. S., 2007, “Thermal radiation in dense nano- and microparticulate media,” Journal of Applied Physics, **102**(7), p. 074316.

[76] Palik E. D., 1985, Handbook of Optical Constants of Solids, Academic Press.

[77] Johnson P. B., and Christy R. W., 1972, “Optical Constants of Noble Metals,” Phys. Rev. B, **6**(12), pp. 4370–4379.

[78] C. Kittel, 1986, Introduction to Solid State Physics, Wiley, New York.

[79] Schelm S., and Smith G. B., 2005, “Evaluation of the limits of resonance tunability in metallic nanoshells with a spectral averaging method.,” Journal of the Optical Society of America. A, Optics, image science, and vision, **22**(7), pp. 1288-92.

[80] Drotning W., 1978, “Optical properties of solar-absorbing oxide particles suspended in a molten salt heat transfer fluid,” Solar Energy, **20**(4), pp. 313-319.

[81] Arm N., and Itaya Y., 1984, “Development of A ‘ Volume Heat-Trap ’ Type Solar Collector Using a Fine-Paticle Semitransparent Liquid Suspensions(FPSS) as a Heat Vehicle and Heat Storage Medium,” Solar Energy, (I), pp. 49-56.

[82] Taylor R. A., Phelan P. E., Otanicar T. P., Adrian R. J., and Prasher R. S., 2011, “Nanofluid Extinction Coefficients for Photothermal Energy Conversion,” Energy Conversion, pp. 1-8.

[83] Ma H., and Dai L. L., 2009, “Synthesis of polystyrene-silica composite particles via one-step nanoparticle-stabilized emulsion polymerization,” Journal of Colloid and Interface Science, **333**(2), pp. 807-811.

[84] Baillis D., and Sacadura J.-F., 2000, “Thermal radiation properties of dispersed media: theoretical prediction and experimental characterization,” Journal of Quantitative Spectroscopy and Radiative Transfer, **67**(5), pp. 327-363.

[85] Osinga T., Lipinski W., Guillot E., Olalde G., and Steinfeld a., 2006, “Experimental Determination of the Extinction Coefficient for a Packed-Bed Particulate Medium,” Experimental Heat Transfer, **19**(1), pp. 69-79.

[86] Kameya Y., and Hanamura K., 2011, “Enhancement of solar radiation absorption using nanoparticle suspension,” Solar Energy, **85**(2), pp. 299-307.

[87] M.C.J.Large, 1996, “Incoherent reflection processes a discrete approach.pdf,” Optics comunication Large.

[88] Halas N. J., Lal S., Chang W.-S., Link S., and Nordlander P., 2011, “Plasmons in strongly coupled metallic nanostructures.,” Chemical reviews, **111**(6), pp. 3913-61.

[89] Fujishima A., and Honda K., 1972, “Electrochemical Photolysis of Water at a Semiconductor Electrode,” Nature, **238**(5358), pp. 37-38.

[90] Kamat P., 2002, “Photophysical, photochemical and photocatalytic aspects of metal nanoparticles,” The Journal of Physical Chemistry B, **106**(32), pp. 7729-7744.

[91] Kwon S., Fan M., Cooper A. T., and Yang H., 2008, Photocatalytic applications of micro- and nano-TiO 2 in environmental engineering.

[92] Djerdj I., Arčon D., Jagličić Z., and Niederberger M., 2008, "Nonaqueous synthesis of metal oxide nanoparticles: Short review and doped titanium dioxide as case study for the preparation of transition metal-doped oxide nanoparticles," Journal of Solid State Chemistry, **181**(7), pp. 1571-1581.

[93] Taylor R. A., Phelan P., Rosengarten G., Gunawan A., Lv W., Otanicar T., and Prasher R. S., 2012, "Critical Review of The Novel Applications and Uses of Nanofluids," Proceedings of the 3rd International Conference on Micro/Nanoscale Heat & Mass Transfer, MNHMT2012-75189, Atlanta, GA.

[94] Jakob M., Levanon H., and Kamat P. V., 2003, "Charge Distribution between UV-Irradiated TiO 2 and Gold Nanoparticles : Determination of Shift in the Fermi Level," Nano Letters, **3**(3), pp. 353-358.

[95] Hirakawa T., and Kamat P. V., 2005, "Charge separation and catalytic activity of Ag@TiO2 core-shell composite clusters under UV-irradiation.," Journal of the American Chemical Society, **127**(11), pp. 3928-34.

[96] Kamat P. V., 2011, "Graphene-Based Nanoassemblies for Energy Conversion," The Journal of Physical Chemistry Letters, **2**(3), pp. 242-251.

[97] Subramanian V., Wolf E. E., and Kamat P. V., 2003, "Influence of Metal / Metal Ion Concentration on the Photocatalytic Activity of TiO 2 -Au Composite Nanoparticles," (25), pp. 469-474.

[98] C.L.Tien, and G.Chen, 1994, "Challenges in condutive and radiative heat tansfer," J. of Heat Transfer, **116**, p. 799.

[99] Monticone S., Tufeu R., Kanaev A. V., Scolan E., and Sanchez C., 2000, "Quantum size effect in TiO 2 nanoparticles : does it exist ?," Applied Surface Science, pp. 565-570.

[100] Du S.-Y., and Li Z.-Y., 2010, "Enhanced light absorption of TiO(2) in the near-ultraviolet band by Au nanoparticles.," Optics letters, **35**(20), pp. 3402-4.

[101] Awazu K., Fujimaki M., Rockstuhl C., Tominaga J., Murakami H., Ohki Y., Yoshida N., and Watanabe T., 2008, “A plasmonic photocatalyst consisting of silver nanoparticles embedded in titanium dioxide.,” Journal of the American Chemical Society, **130**(5), pp. 1676-80.